

COVER SHEET

Name: Transition Form Factor of the η' Meson with CLAS12

Spokesperson: Michael C. Kunkel

Contact: m.kunkel@fz-juelich.de

Proposed Run-Time: 80 Days

Proposed RunGroup: A

Equipment: Standard CLAS

Trigger: Standard CLAS Electron Trigger

Settings: 75% Torus field

Similar Proposals:

- E12-11-005: Meson spectroscopy with low Q^2 electron scattering in CLAS12
- E12-06-108: Hard Exclusive Electroproduction of π^0 and η with CLAS12
- E12-12-001: Timelike Compton Scattering and J/ψ photoproduction on the proton in e^+e^- pair production with CLAS12 at 11 GeV

Impact of Run-Group:

A CLAS Proposal for PAC44

Transition Form Factor of the η' Meson with CLAS12

M. C. Kunkel^{*†1}, L. Guo³, C. Hanhart¹, B. Kubis⁴, D. Lersch¹, J. Ritman¹, S. Schadmand¹, X. Song¹, A. Wirzba¹

¹Forschungszentrum Jülich, Jülich (Germany)

³Florida International University (U.S.A.)

⁴University of Bonn (Germany)

Abstract

Dalitz decays are radiative decays in which the photon is virtual and subsequently produces an electron positron pair, $P \rightarrow l^+l^- X$. Such decays serve as an important tool used to reveal the internal structure of hadrons and the interaction mechanisms between photons and hadrons. Furthermore, assuming point-like particles, the electromagnetic interaction is calculable within QED by the Kroll-Wada formula. Transition form factors quantify modifications of the point-like photon-meson vertex due to the transitions and interactions of the meson. The transition form factor can be characterized as $|F(q^2)|$, where q^2 is the square of the invariant mass of the lepton pair, and can be determined by comparing QED predictions to the experimentally measured rate. The goal of this analysis is to determine the transition form factor for the η' meson. This measurement will aid in limiting the largest uncertainty of the Standard Model prediction for hadronic quantum corrections in the muon anomaly.

From previous CLAS analyses using the g12 data set, it was shown that measurements of the time-like transition form factor were achievable, but without the statistical precision needed to be competitive. Therefore, we propose to use CLAS12 to focus on the dilepton decay channels from the reactions $ep \rightarrow e'p\eta'$, where $\eta' \rightarrow e^+e^-\gamma$. Preliminary studies using the CLAS12 simulation suite have shown that a beam time of 80 days, at full luminosity, will accumulate a data sample at least one order of magnitude larger in statistics than the most current $\eta' \rightarrow e^+e^-\gamma$ measurement.

^{*}Contact person, email: m.kunkel@fz-juelich.de

[†]Spokesperson

Contents

1	Introduction	2
1.1	Motivation	3
1.2	History	5
1.3	Proposal	5
2	Kinematics	6
2.1	The Dalitz Decay	7
2.2	Form Factor	7
2.3	Background from Real Photon Pair Production	9
3	Current Experimental Measurements	12
3.1	Previous CLAS analyses	14
3.1.1	G12 Lepton and Neutral Trigger Setup	14
3.1.2	G12 Detection of e^+e^- Events	16
3.1.3	$\eta' \rightarrow e^+e^-\gamma$ with CLAS g12	24
4	Measurement	24
4.1	Simulation and Reconstruction	25
4.1.1	Trigger Requirements	25
4.1.2	Detection of e^+e^- Events	25
4.1.3	Particle Identification	25
4.1.4	Acceptance	26
4.2	Calculating the Expected Yield	28
4.3	Acceptance at 100% Torus field	32
4.4	Expected Systematic Uncertainties	33
5	Beam Time Request	34
	BIBLIOGRAPHY	35
	APPENDICES	39

1 Introduction

Current measurements on the determination of the transition form factor have been performed in the space-like region ($q^2 < 0$) in collider experiments. However, due to experimental limitations (e.g. π^\pm contamination in lepton sample, low branching fractions, external conversion contamination), transition form factors in the time-like region ($q^2 > 0$) have not yet been precisely determined. Recent measurements of the time-like transition form factor for $\eta' \rightarrow e^+e^-\gamma$ have been performed by the BESIII collaboration with insufficient statistical precision to distinguish between different theoretical approaches.

1.1 Motivation

While very successful in many aspects, the Standard Model of particle physics (SM) leaves a few important questions unanswered. On the one hand, it predicts an amount of matter that survived annihilation after the Big Bang that is many orders of magnitude less compared to what is observed. In addition, since masses of matter particles appear as parameters in the SM, it does not provide any understanding why the values of these masses span so many orders of magnitude. In addition, within the SM, phenomena like Dark Matter and Dark Energy can not be explained. These and some more issues suggest that there must be physics beyond the SM, and many experiments world-wide hunt for signals of it.

One of the currently most promising candidates to provide a signal for physics beyond the SM is the muon anomaly. It is a low-energy observable, which can be both measured and computed to high precision [1, 2]. “The anomaly is defined by $a_\mu = (g - 2)/2$, where the Landè g -factor is the proportionality constant that relates the spin to the magnetic moment. For the muon, as well as for the electron and tauon, the anomaly a differs slightly from zero (of order 10^{-3}) because of radiative corrections. In the Standard Model, contributions to the anomaly come from virtual ‘loops’ containing photons and the known massive particles.” [3] The present experimental value $a_\mu^{\text{EXP}} = 1\,165\,920\,89(63) \times 10^{-11}$ comes from the BNL E821 experiment [4]. This value deviates from the SM prediction by about 3 standard deviations $\Delta a_\mu^{(\text{EXP-SM})} = (287 \pm 80) \times 10^{-11}$ [5] or $= (261 \pm 78) \times 10^{-11}$ [6], depending on how the leading-order hadronic contributions are evaluated. While this discrepancy is not large enough to claim a failure of the SM, it is currently the largest deviation of a SM prediction from an experimental observable. This alone justifies the efforts currently taken to improve both the theoretical as well as the experimental value. New measurements are planned within the next four years at Fermilab/USA [7] and also at JPARC/Japan [8]. The goal of the measurements is to reduce the uncertainty by a factor of four. In parallel the SM prediction needs to be improved in accuracy by at least a factor of two to establish a deviation from the SM for the first time.

The largest uncertainty of the SM prediction comes from the hadronic quantum corrections [1]. At the level of accuracy that is relevant at the moment the hadronic contributions can be split up into the hadronic vacuum polarization (HVP), displayed on the left-hand side of figure 1, and the hadronic light-by-light scattering (HLbL), displayed in the middle of Fig. 1. The most important contribution to the latter comes from the pseudoscalar pole contributions, displayed explicitly on the right-hand side of Fig. 1. For those one expects that the contribution should be largely saturated by the lightest exchange particles, namely the π^0 , the η and the η' .

Concerning the SM prediction for a_μ HLbL is suppressed relative to HVP by one power of the electromagnetic fine structure constant [1, 9]. Un-

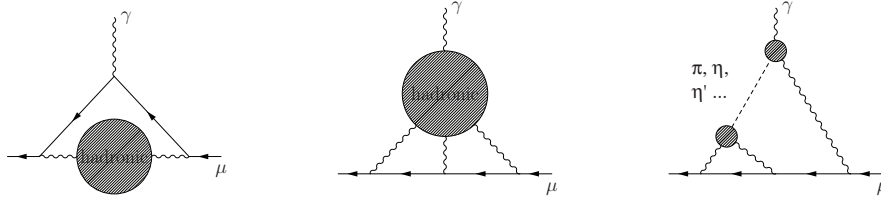


Figure 1: Hadronic contributions to a_μ : hadronic vacuum polarization (left diagram), hadronic light-by-light scattering (middle), pion-pole contribution to hadronic light-by-light scattering (right). Full lines with an arrow denote muons, wiggly lines photons, the dashed line a pseudo-scalar meson and shaded blobs a non-pointlike hadronic substructure. The upper blob in the right diagram corresponds to Fig. 2b, while the lower blob corresponds to the double Dalitz decay.

fortunately at present it is not possible to straightforwardly calculate the contributions shown in Fig. 1 from first principles analogously to, e.g., the QED corrections, since both processes concern low-energy corrections, i.e. non-perturbative physics. Thus the prime candidate for a SM calculation of hadronic corrections seems to be lattice QCD [10]. However, it is not expected that lattice QCD results for HPV will reach the required accuracy in the foreseeable future. For the HLbL only preliminary lattice-QCD calculations have been reported [11]. In view of the challenges to determine a four-point function that includes in addition disconnected diagrams it is not clear yet when a profound lattice calculation with controlled uncertainties and a reliable error estimate will be available.

Fortunately there is an alternative way to quantify hadronic corrections. It requires both theoretical as well as experimental efforts: Dispersion theory provides a link between particular hadronic cross sections and a_μ —for a discussion of the HVP in this context see Ref. [1], while for HLbL we refer to Refs. [12, 13, 14, 15]. In particular for the latter contribution it allows one to calculate from the transition form factors of the kind $\pi^0, \eta, \eta' \rightarrow \gamma^* \gamma^*$ the corresponding piece for the meson pole contribution as displayed in the right most diagram of Fig. 1. The measurements proposed here provide important information towards the necessary input needed for the evaluation of the HLbL contribution, since $\eta' \rightarrow \gamma^* \gamma$ gives the single off-shell form factor of the η' and $\phi \rightarrow \eta \gamma$ additionally provides information on the isoscalar piece of $\eta \rightarrow \gamma^* \gamma$ in a different kinematic regime. Additional information on the η and η' form factors can be found from the dispersive methods outlined in Refs. [16, 17, 18, 19, 20]. It appears to be realistic that this joined effort of theory and experiment will provide the improvements necessary to push the SM calculation towards the required accuracy. For the η' pole contribution a precision of 15% on the HLbL correction are feasible. [21].

1.2 History

In the year 1951, Richard Dalitz published a letter [22] in which he calculated the rate for the π^0 decaying into an electron-positron pair (dilepton) and a photon, $\pi^0 \rightarrow e^+e^-\gamma$. The calculation assumed that the decay proceeded through a two-photon decay in which one of the photons was virtual and converted into an electron-positron pair. This kind of reaction is now known as Dalitz decay. The experimental evidence of this decay process was first observed in emulsion plates exposed to the Chicago cyclotron in 1952 [23] and a number of experiments performed over the next ten years verified Dalitz's hypothesis that the $\pi^0 \rightarrow e^+e^-\gamma$ decay resulted from emission of a virtual photon [24, 25, 26]. A few years later N. Kroll and W. Wada calculated the framework for Dalitz decays within the QED framework [27], and extended the framework to double Dalitz Decays, in which the π^0 decays into two electron-positron pairs via emission of two virtual photons.

Throughout the following years, much work was done to extend the framework of Dalitz decays to heavier mesons, such as η , ω , η' , and ϕ . With numerous experimental data taken, it was shown that the shape of the dilepton mass spectrum deviated from the QED predictions. Such deviations are attributed to the meson not being point-like, as calculated in QED, but instead to the internal structure of the meson. The virtual photon, that decayed into a dilepton pair, has the ability to probe the structure of meson because, like its on-shell counterpart, emission of a virtual photon is radiation, which decouples from any strong interaction within the meson when the meson transitions into its decay. Therefore, the information of the transition is encoded into the virtual photon, known as the Transition Form Factor (TFF), and can be characterized as $|F(q^2)|$, where q^2 is the square of the invariant mass of the lepton pair. The transition form factor can be determined by comparing QED predictions to the experimentally measured rate. Previous experimental results will be shown in Sec. 3.

1.3 Proposal

In this proposal we present an experiment to study the η' meson which decays via Dalitz decay, $\eta' \rightarrow e^+e^-\gamma$. The η' is produced via electro-production, $ep \rightarrow ep\eta'$ in Hall B, using the CLAS12 detector. The CLAS12 detector will be used to identify and measure the e^+e^- decay products by means of the High Threshold Cherenkov Counter (HTCC), Pre-Calorimeter (PCAL) and Electromagnetic Calorimeter (EC). The combination of HTCC+PCAL+EC can provide a rejection factor for single e^\pm/π^\pm of up to 10^5 for momenta less than 4.9 GeV/c with $\approx 100\%$ efficiency. For dileptons (e^+e^- pairs), this rejection factor will be $\approx 10^{10}$, which enables dilepton studies for branching ratios $\approx 10^{-7}$. Precise determination of momenta and angles of the e^+e^- decay products are the key features available to CLAS12. The momentum

and angle of final state photons will be determined in CLAS12 by using the PCAL and EC. Consequently, the photon in the process $\eta' \rightarrow e^+e^-\gamma$ will be detected. This proposal is organized as follows. In Section 2, an explanation of the kinematics of the decay processes will be given as well as kinematics of main competing backgrounds. In Section 3, we summarize the current knowledge of Dalitz decays and transition form factors, challenges in dilepton signal quality. Also a brief discussion on past CLAS analysis will be given, along with and how the CLAS12 detector can surpass the current challenges in measuring a TFF, for η' , of low statistical error. In Section 4 a description of the analysis techniques that have been used and will be used in a CLAS12 measurement. Also in Section 4, an explanation of the Monte-Carlo simulations that were performed to extract the acceptances will be given as well as a calculation of expected yield and a validity check on the expected yield from previous CLAS analyses. In Section 5 we present the beam time request.

2 Kinematics

The channel proposed to be studied is

$$e(k) + p(p) \rightarrow e'(k') + p'(p') + \eta'(\nu) \quad (1)$$

where k, k', p, p' are the four-momenta of the incident lepton, outgoing lepton, target proton and scattered proton respectively. The virtual photon in the production is defined as $q = k - k'$ with energy $v = \frac{pq}{m_p} = E - E'$. The quantity $\eta'(\nu)$ is the electro-produced meson. Production mechanisms of similar mesons have been already proposed in previous proposals [28, 29] and are scheduled to run in conjunction with RunGroupA, the same run group requested for in this proposal. The main decays studied for this proposal are:

$$\eta' \rightarrow \gamma\gamma \rightarrow e^+e^-\gamma \quad (2)$$

$$\eta' \rightarrow \gamma\gamma^* \rightarrow \gamma e^+e^- \quad (3)$$

i.e. when a pseudoscalar meson, $P_p(\eta')$, decays via two photons (Eq. 2) and one photon converts into an e^+e^- pair due to E.M. processes through matter, this is conventionally known as external conversions. This decay channel will be the main background contribution and is further discussed in Sec 2.3. The Dalitz decay (Eq. 3), or internal conversion, is when the $P_p(\eta')$ decays via a real photon and a virtual photon, which decays into an e^+e^- pair. Figure 2 illustrates the Feynman diagrams for the pseudoscalar “two photon decay” and “Dalitz decay”. A full derivation of the external conversion and Dalitz decay are given in the Appendix A.

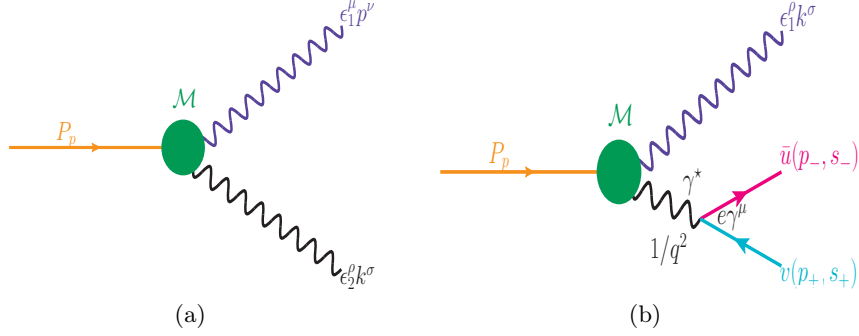


Figure 2: Feynman diagram of $P_p(\eta')$ two photon decay (a), ϵ_1 and ϵ_2 are the polarizations, p and k are 4-momenta of the photons. Feynman diagram of $P_p(\eta')$ Dalitz decay (b), the variable s_{\pm} are the spin helicities of the outgoing leptons l^{\pm} with 4-momenta p_{\pm} and ϵ is the polarization of the outgoing photon with 4-momenta k . In both diagrams \mathcal{M} is the form factor.

2.1 The Dalitz Decay

The Dalitz decay of mesons is dependent on the spin of the meson. For pseudoscalar meson the decay rate is derived in A.2 and is expressed as:

$$\frac{d\Gamma_{e^+e^-\gamma}}{\Gamma_{\gamma\gamma}dq^2} = \frac{2\alpha}{3\pi} \frac{1}{q^2} \left(1 - \frac{q^2}{m_p^2}\right)^3 \left(1 + \frac{2m_l^2}{q^2}\right) \left(1 - \frac{4m_l^2}{q^2}\right)^{\frac{1}{2}} \quad (4)$$

which is the Kroll-Wada equation found in [27, 30]. An example of QED expectation for η' is shown in Fig. 3.

2.2 Form Factor

It has been experimentally observed that the shape of the dilepton mass spectrum deviates significantly from the QED predictions, displaying a rise at larger dilepton mass. Therefore, the form factor $M_P(p^2, k^2 = 0)$ or $M_P(p_1^2, p_2^2)$ can be written as follows:

$$M_P \rightarrow M'_P \times |F(q^2)|, \quad (5)$$

where M'_P is the decay constant of two photons or η photon (as mentioned in Sec. A.1), while $|F(q^2)|$ is called the transition form factor, which defines the electromagnetic space structure of the meson. According to that, the $\eta' \rightarrow e^+e^-\gamma$ decay rate modifies as;

$$\frac{d\Gamma_{e^+e^-\gamma}}{\Gamma_{\gamma\gamma}dq^2} = \frac{2\alpha}{3\pi} \frac{1}{q^2} \left(1 - \frac{q^2}{m_p^2}\right)^3 \left(1 + \frac{2m_l^2}{q^2}\right) \left(1 - \frac{4m_l^2}{q^2}\right)^{\frac{1}{2}} |F(q^2)|^2, \quad (6)$$

First observations were described with standard vector meson dominance (VMD) where the virtual photon can stem from intermediate vector mesons. The value of $|F(q^2)|$ can be directly measured by comparing QED predictions to the measured rate [30].

$$\frac{d\Gamma(A \rightarrow B + l^+l^-)}{dq^2\Gamma(A \rightarrow B\gamma)} = \left[\frac{d\Gamma}{dq^2} \right]_{\text{QED}} \cdot |F(q^2)|^2 \quad (7)$$

or by performing a line shape analysis on the l^+l^- invariant mass using assumptions on the structure of $|F(q^2)|$. One such assumption for $|F(q^2)|$ is the dipole approximation from the VMD model, which can be parametrized as:

$$F(q^2) = \frac{1}{1 - q^2/\Lambda^2} \quad (8)$$

where the parameter Λ corresponds to the mass for the effective contributing vector meson.

The slope of the transition form factor, b , is defined as:

$$b \equiv \frac{dF}{dq^2} \Big|_{q^2=0}. \quad (9)$$

and characterizes the intrinsic spatial charge radius for the η' meson. Several theoretical approaches have been developed to describe the transition form factor and are listed in Tab. 1.

Approach	slope parameter ($b_{\eta'}$)
Dispersion	$1.53^{+0.15}_{-0.08} \text{GeV}^{-2}$
Chiral Perturbation	1.6GeV^{-2}
VMD	1.45GeV^{-2}

Table 1: Theoretical approaches to describe the transition form factor

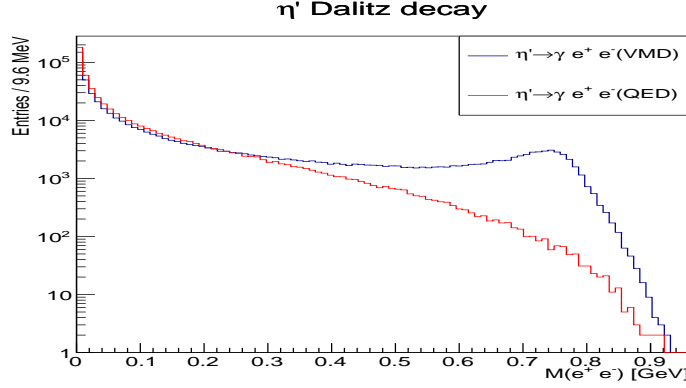


Figure 3: Example of Dalitz spectra for η' using only QED(red) and the deviation from QED using the VMD parameterization(blue) with 500K Dalitz events generated.

2.3 Background from Real Photon Pair Production

When a photon travels through matter at energies greater than 100 MeV, it can convert into an electron-positron pair via $\gamma Z \rightarrow Z e^+ e^-$. The cross section for this process can be written as;

$$\sigma_{\gamma \rightarrow e^+ e^-} = \frac{A}{N_A \rho \lambda_\gamma}, \quad \lambda_\gamma = \frac{9}{7} X_0 \quad (10)$$

where λ is the interaction length, or mean free path, ρ is the density of the material, N_A is Avogadro's number and A is the atomic mass of the material. The probability of pair production to occur is solely based on X_0 , the radiation length of the medium, and the distance, x , the photon travels inside the medium. This probability can be expressed as;

$$\frac{dP}{dx} = \frac{1}{\lambda_\gamma} \exp\left(\frac{-x}{\lambda_\gamma}\right). \quad (11)$$

The probability of pair production related to a photon, from $\eta' \rightarrow \gamma\gamma$, traveling through 5 cm of liquid hydrogen, ℓ_{H_2} , is shown in Fig. 4. The branching ratio, $\frac{\Gamma_{\eta' \rightarrow e^+ e^- \gamma}}{\Gamma_{\eta' \rightarrow \gamma\gamma}} = 2.13 \cdot 10^{-2}$, was measured by [31] and is also consistent with preliminary CLAS measurements [32]. Using this branching ratio, the probability of pair production normalized by the amount of Dalitz decays, $\eta' \rightarrow \gamma\gamma \rightarrow e^+ e^- \gamma / 100 \eta' \rightarrow e^+ e^- \gamma$, is calculated and also shown in Fig. 4. Since CLAS12 has a vertex resolution of ≈ 1 mm the probability of pair production traveling through 10 mm is shown in Fig. 5. Therefore, a 1 mm cut on the primary vertex will yield a contamination of \approx one externally converted $e^+ e^-$ from $\eta' \rightarrow \gamma\gamma \rightarrow e^+ e^- \gamma$ per 100 Dalitz decays. The exter-

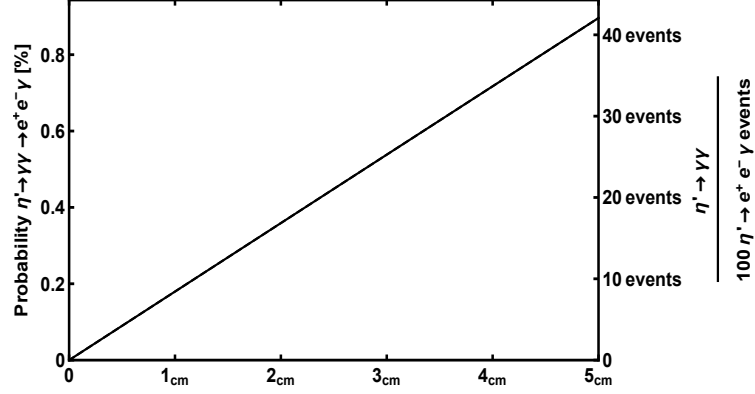


Figure 4: (Left axis) Probability of pair production, $\gamma \rightarrow e^+e^-$; (Right axis) number of $\eta' \rightarrow \gamma\gamma \rightarrow e^+e^-\gamma / 100\eta' \rightarrow e^+e^-\gamma$ as a function of distance in liquid hydrogen.

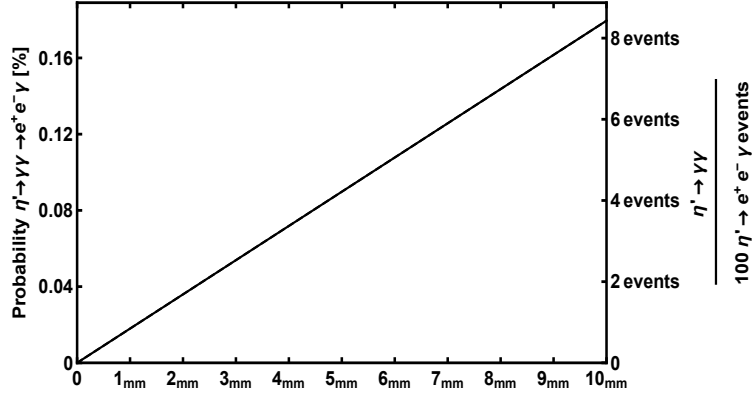


Figure 5: (Left axis) Probability of pair production, $\gamma \rightarrow e^+e^-$; (Right axis) number of $\eta' \rightarrow \gamma\gamma \rightarrow e^+e^-\gamma / 100\eta' \rightarrow e^+e^-\gamma$ as a function of distance in liquid hydrogen.

nal conversion process mimics the Dalitz decay $\eta' \rightarrow e^+e^-\gamma$, described in Sec. A.2. Since there are two photons with equal probability of conversion for $\eta' \rightarrow \gamma\gamma$, the total probabilities shown is for when either photon externally converts. From multiple scattering effects the e^+e^- from a converted photon will obtain a mass distribution. Simulations of photons from η' radiative decays traversing through 1 mm of ℓH_2 show that the e^+e^- can obtain a maximum mass of ~ 0.14 GeV.

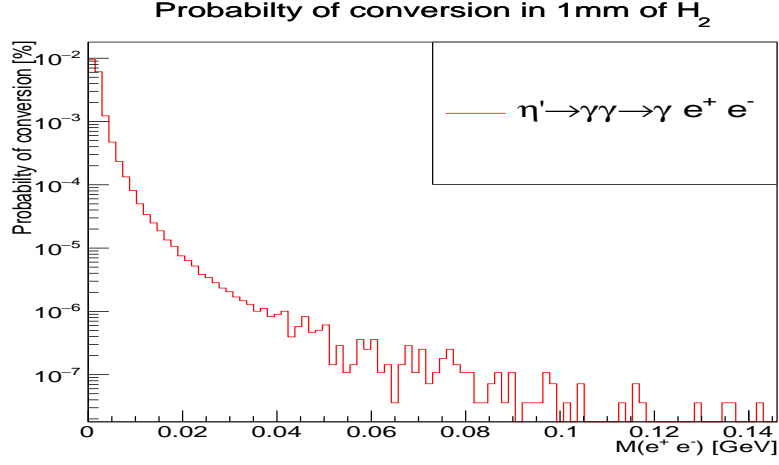


Figure 6: Probability of pair production in 1 mm of ℓH_2 for $\eta' \rightarrow \gamma\gamma$ vs. $M(e^+e^-)$.

The CLAS12 detector will have vertex resolution of ~ 1 mm, therefore the amount of contamination of externally converted pairs will be minimized by the vertex position of the e^+e^- pair. An example of the total contamination, in the Dalitz spectrum, from external conversion within 1 mm of the primary vertex can be seen in Fig. 7. It should be noted that the result in Fig. 7 is an approximate calculation and not a simulation.

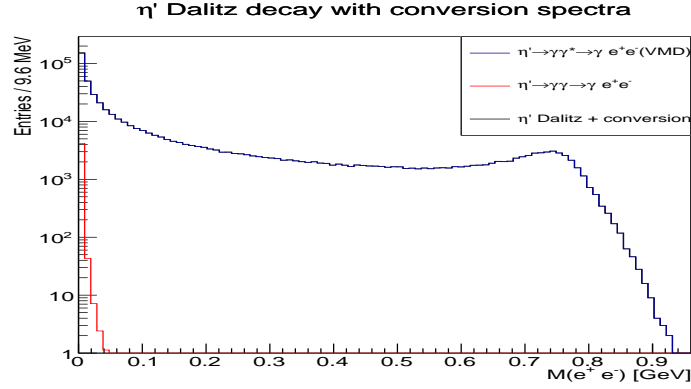


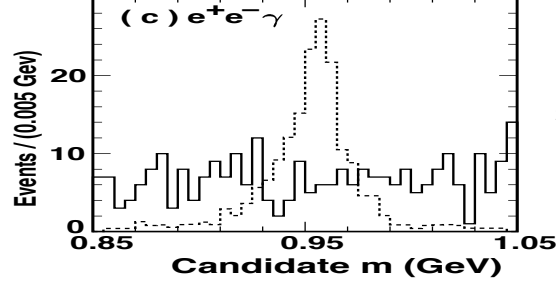
Figure 7: Example of Dalitz and conversion spectra for η' with 500K Dalitz events generated and $\sim 2.35 \cdot 10^7$ $\eta' \rightarrow \gamma\gamma$ generated.

3 Current Experimental Measurements

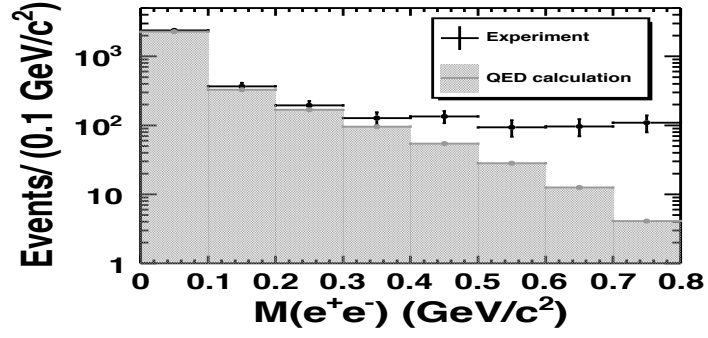
Several experimental groups are currently investigating transition form factors in the time-like regime, including, but not limited to;

- TRIUMF $\pi^0 \rightarrow e^+e^-\gamma$ [33]
- A2 Collaboration $\eta \rightarrow e^+e^-\gamma$ [34, 35]
- Multiple Groups $\omega \rightarrow \pi^0\mu^+\mu^-$ [36, 37, 38]
- CLEO Collaboration $\eta' \rightarrow e^+e^-\gamma$ [39]
- Lepton-G $\eta' \rightarrow \mu^+\mu^-\gamma$ [40]
- BESIII Collaboration $\eta' \rightarrow e^+e^-\gamma$ [41]
- KLOE Collaboration $\phi \rightarrow e^+e^-\eta$ [42] .

The branching ratio of $\eta' \rightarrow e^+e^-\gamma$ remained an upper limit, Fig. 8, until the BESIII collaboration finally measured it using 1.31 billion $J/\psi \rightarrow \gamma\eta' \rightarrow \gamma\gamma e^+e^-$. From the BESIII data sample, Fig. 8, only 894 $\eta' \rightarrow e^+e^-\gamma$ events were recorded which lead to a determination of the branching ratio $\Gamma_{\eta' \rightarrow e^+e^-\gamma} = 4.69 \pm 0.2(\text{stat.}) \cdot 10^{-4}$ and a slope parameter, Eq. 9, $b = 1.60 \pm 0.17(\text{stat.})$ which is consistent with the measurement from Lepton-G ($1.7 \pm 0.4(\text{stat.})$). The slope parameter measured by BESIII and Lepton-G, which is the essential measurement needed for the HLbl contribution, is not sufficient to distinguish between different theoretical approaches listed in Tab. 1. Some of the obstacles for not measuring the $\eta' \rightarrow e^+e^-\gamma$ was the low branching ratio, pion contamination and low electron PID efficiency. These obstacles will be mitigated with CLAS12 by the high luminosity and excellent dilepton identification.



(a)



(b)

Figure 8: (a) Missing mass off of the proton for $\eta' \rightarrow e^+e^-\gamma$ from the CLEO collaboration [39], solid line(data), dashed(MC expectation). (b) Counts of $M(e^+e^-)$ from the first published observation of the $\eta' \rightarrow e^+e^-\gamma$ by BE-SIII [31].

3.1 Previous CLAS analyses

The LMD (Light Meson Decay) group of CLAS was established to investigate the decay properties of light mesons. Two experiments in CLAS are currently being analyzed in the LMD group. The g12 experiment, performed with CLAS, is one experiment chosen due to its ability to identify leptons with the use of the Cherenkov detectors (CC). The g12 experiment produced a data set of photon-induced reactions. Fortunately, the Cherenkov Counters were filled with perflourbutane (C_4F_{10}) and a trigger consisting of a coincidence between the (ST·TOF)(CC·EC), allowing the study of dilepton reactions throughout the entire beam energy range $1.15 \text{ GeV} < E_\gamma < 5.45 \text{ GeV}$. The g12 experiment ran for 44 days however, the trigger that allowed for e^+e^- identification was established for ~ 29 days of beam-time. Using approved dilepton identification [43], preliminary analyses of g12 involving dileptons include the decays:

- $\Delta \rightarrow pe^+e^-$ (Transition form factor)
- $\eta \rightarrow e^+e^-\gamma$ (Transition form factor)

while advanced analyses involving dileptons include:

- $\pi^0 \rightarrow e^+e^-\gamma$ (Differential Cross-Section)
- $\omega/\rho \rightarrow e^+e^-$ (Interference of ω/ρ)
- $\omega \rightarrow e^+e^-\pi^0$ (Transition form factor)
- $\eta' \rightarrow e^+e^-\gamma$ (Transition form factor / branching ratio)

The g12 $\eta' \rightarrow e^+e^-\gamma$ analysis provided CLAS its first look at the possibility of measuring the branching ratio and transition form factor.

3.1.1 G12 Lepton and Neutral Trigger Setup

In g12, since the CC was filled with gas, it was possible to include the CC as a component of the trigger. There were three trigger “bits” used for lepton identification in g12 as listed in Tab. 2. Each “bit” used a (EC·CC) configuration to identify leptons. The (EC·CC) configuration required a coincidence between the electromagnetic calorimeter and the Cherenkov subsystems. This coincidence was established by using the voltage sum of the CC for a sector and the voltage sum of the EC for the same sector and comparing each sum to a preset threshold described in Tab. 3. The EC voltage sum threshold comparison is done on both the EC_{inner} and EC_{total} which are the EC voltage signals for the energy deposited in the inner layer and in all layers. The labels of photon or electron specified in Tab. 3 are not actual photons or electrons, but were considered a first-order approximation for detection. The particle identification is done at the analysis level. The method for determining the

g12 runs 56595–56607, 56648–57323			
bit	definition	L2 multiplicity	prescale
1	MORA·(ST·TOF)	1	1000/300
2	MORA·(ST·TOF)×2	2/–	1
3	MORB·(ST·TOF)×2	2	1
4	ST·TOF	1	1000/300
5	(ST·TOF)·EC×2	1	1
6	(ST·TOF)·(EC·CC)	2	1
7	MORA·(ST·TOF)·(EC·CC)	–	1
8	MORA·(ST·TOF)×2	–	1
11	(EC·CC)×2	–	1
12	(ST·TOF)×3	–	1

Table 2: Trigger configuration for g12 runs from 56595 to 56607 and 56648 to 57323.

(EC·CC) does not allow for multiple lepton triggering in the same sector. Determining multiple leptons in the same sector is done at the analysis level.

The “bit 6” trigger configuration, (ST·TOF)·(EC·CC) requires a Start-Counter (ST) and Time-of-Flight (TOF) coincidence along with a coincidence between the electromagnetic calorimeter and the Cherenkov subsystems described above. The (ST·TOF) configuration of “bit 6” did not have to be in the same sector as the (EC·CC) configuration of “bit 6”. The “bit 11” trigger configuration, (EC·CC)×2 requires two coincidences between the electromagnetic calorimeter and the Cherenkov subsystems described above, in two different sectors.

The “bit 5” trigger configuration was also established as a lepton trigger. It required EC hits in two sectors. The “bit 5” trigger configuration was also established to analyze physics involving two or more neutral particles accompanied with a charged track, such as exclusive π^0 production in which the π^0 decays via 2 photons. The method for “bit 5” voltage sum comparison is identical to the EC voltage sum of “bit 6” and “bit 11”

It should be noted that none of the lepton triggers required a MOR signal, allowing for physics involving leptons to be measured starting from g12’s lowest tagger detection value of 1.142 GeV.

EC		CC
"photon"	"electron"	
50/100 mV	60/80 mV	20/20 mV
150/300 MeV	180/240 MeV	~0.4 photo-electrons

Table 3: Threshold values for the electromagnetic calorimeter (EC) and Cherenkov counter (CC) during the g12 running period. EC thresholds are shown as *inner/total*, and CC thresholds are shown as *left/right*.

3.1.2 G12 Detection of e^+e^- Events

The g12 experiment derived a set of conditions for identifying electron/positrons pairs in CLAS by employing specific cuts to the number of photo-electrons (NPE) detected in the CC, a match in azimuthal angle ϕ from a charged track in the Drift Chambers (DC) to the ϕ of the CC, as well as comparing the momentum of the charged track to the energy deposited in the EC. These cuts can be found in Tab. 4. To validate the g12 electron/positron PID, a

Subsystem	Quantity	Cut
CC	# of photo-electrons (NPE)	$NPE > 2.5$
	$DC \phi$ & $CC \phi$	$DC \phi = CC \phi$
EC	q^\pm momentum threshold (p_{thres}) & EC deposited energy (E_{calo})	$p_{thres}^{high} < E_{calo} < p_{thres}^{low}$

Table 4: Cuts applied to the CC and EC to perform electron/positron PID . Table source: [44]

comparison of the CC and EC quantities was performed for all charged tracks CC/EC hit signatures and while selecting events from π^0 decay. To separate the π^0 events from the $\pi^+\pi^-$ events, all charged pions were assigned the mass of electrons and cuts were placed on the missing energy of $\gamma p \rightarrow p e^+ e^-$ as well as a cut on the missing mass squared of $\gamma p \rightarrow p$, values found in Tab. 5. A graphical depiction of the cuts applied to separate π^0 events from the $\pi^+\pi^-$ events is seen in Fig. 9. The values of the threshold momentum

Cut Topology	Topology Quantity	Value
$\gamma p \rightarrow p e^+ e^-$	Missing Energy (M_E)	$> 0.075 \text{ GeV}$
$\gamma p \rightarrow p$	Missing mass squared (M_x^2)	$< 0.0779 \text{ GeV}^2$ for π^0 events
		$> 0.0779 \text{ GeV}^2$ for $\pi^+\pi^-$ events

Table 5: Cuts applied to separate π^0 events from $\pi^+\pi^-$ events. Table source: [44]

are calculated from empirical studies and are based upon calculations using the momentum obtained from the DC p under the following criteria;

$$p_{\text{thres}}^{\text{low}} = \alpha p * (p + EC_{P_LO})/p$$

$$p_{\text{thres}}^{\text{high}} = \alpha p * (p + EC_{P_HIGH})/p$$

where $EC_{P_LO} = -0.3$, $EC_{P_HIGH} = 0.5$ and

$$\alpha p = \begin{cases} .23 * p + .071p^2 - .032p^3, & p < 1.0 \text{ GeV} \\ 0.272p, & p > 1.0 \text{ GeV} \end{cases}$$

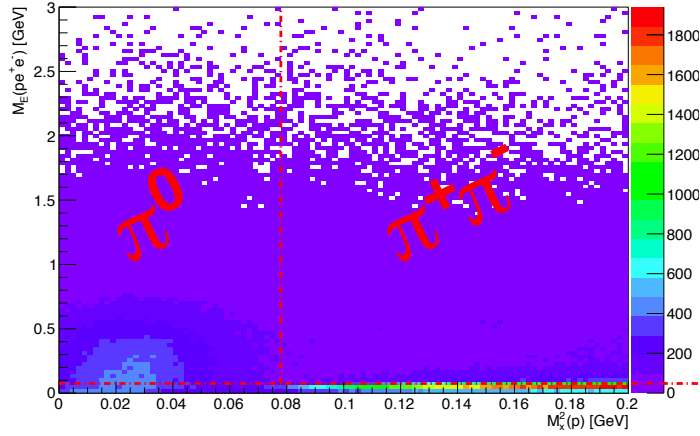


Figure 9: Plot of missing mass squared of off proton (horizontal) vs. missing energy of proton e^+e^- (vertical). The red dashed vertical line depicts the $\pi^+\pi^-$ threshold mass cut while the horizontal red dashed line represents the missing energy cut-off used to separate $\pi^+\pi^-$ from π^0 . Image source: [44, 43]

CC Comparison The NPE measured by the CC for all positron/electron (e^+/e^-) candidates can be seen in Fig 10. The sharp decline prior to 2.5 NPE is due to photo-electrons created by electron/positrons, pions traveling through the CC or pions producing delta-electrons which pass through the CC. Delta-electrons are created as an effect of the ionization of gases that could be present when the pion travels through the DC. These types of electrons are typically lower in momentum than the electrons obtained from particle decays in CLAS and thus should emit less NPE per unit length.

Through mass conservation the particles for the π^0 events must be e^+e^- pairs. In comparison to fig. 10, fig. 11 plots the NPE measured by the CC for all ee^+e^- pairs for π^0 events selected as shown in fig. 9. It can be seen that the sharp decline prior to NPE = 2.5 is reduced leaving mostly electrons or positrons signatures in the CC concluding that the g12 CC NPE cut is valid

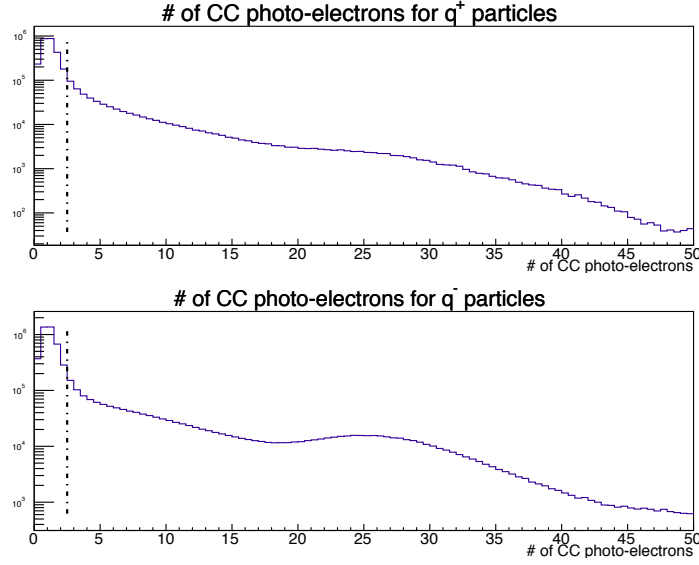


Figure 10: Plot of NPE measured by CLAS CC subsystem for positron/electron candidates top/bottom respectively. The dashed dotted vertical line depicts the cut applied if using the g12 lepton PID scheme. Image source: [44]

for identifying e^+e^- pairs while rejecting $\pi^+\pi^-$ pairs. Using the current cuts of NPE and hit angle, the suppression of di-leptons was sufficient without including additional cuts on the CC such as a timing comparison to the TOF.

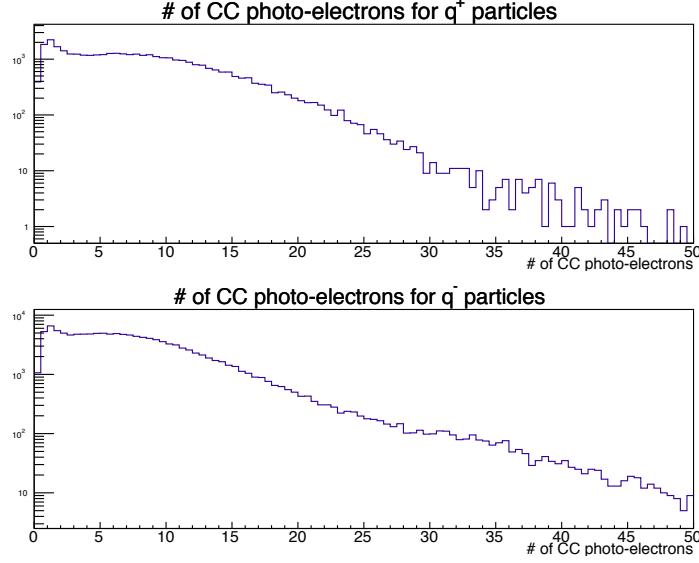


Figure 11: Plot of NPE measured by CLAS CC subsystem when selecting π^0 events seen in Fig 9, positron/electron candidates top/bottom respectively. Image source: [44]

EC Comparison Similarly to the CC comparison, figures 12, 13, 16, 17 depict the $p_{\text{thres}}^{\text{low}}$ and $p_{\text{thres}}^{\text{low}}$ cuts listed in Tab. 4 for the q^- and q^+ tracks respectively. After π^0 event selection, seen in figures 14, 15, 18, 19, the bulk of e^+e^- events reside within the region of the cut acceptance therefore it is evident that the g12 EC cuts are valid for identifying e^+e^- pairs. The following four plots are for electron(e^-) PID validation of the g12 EC cuts described in Tab. 4.

Figures 16–19 are for positron (e^+) PID validation of the g12 EC cuts described in Tab. 4.

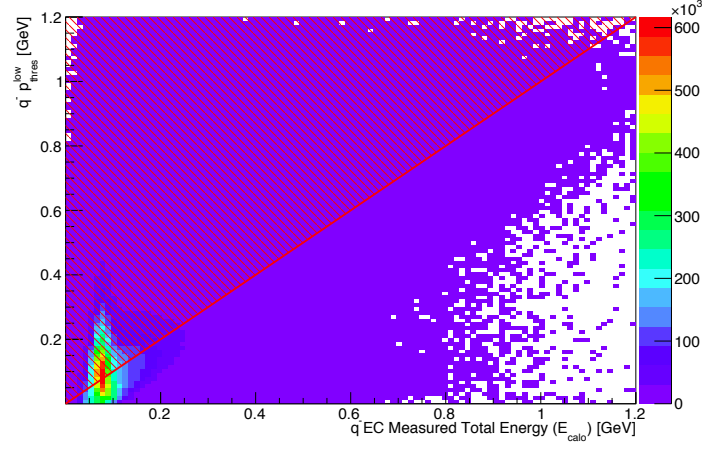


Figure 12: Plot of energy deposited measured by EC vs. track momentum $p_{\text{thres}}^{\text{low}}$ for negative charged tracks. The red region depicts the cut that would reject events in the g12 lepton EC PID scheme. Image source: [44]

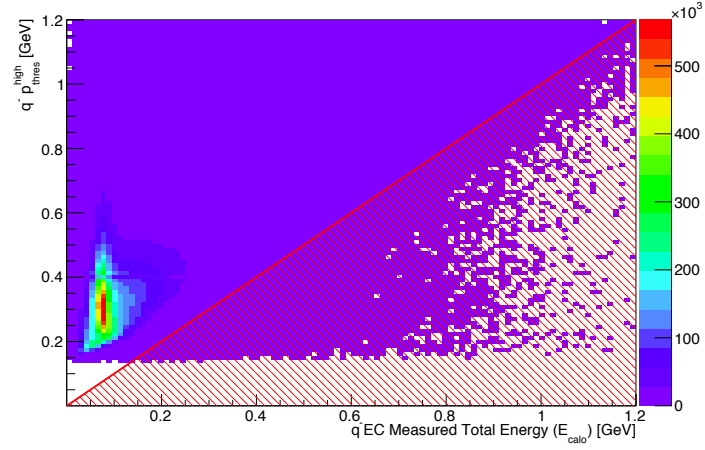


Figure 13: Plot of energy deposited measured by EC vs. track momentum $p_{\text{thres}}^{\text{high}}$ for negative charged tracks. The red region depicts the cut that would reject events in the g12 lepton EC PID scheme. Image source: [44]

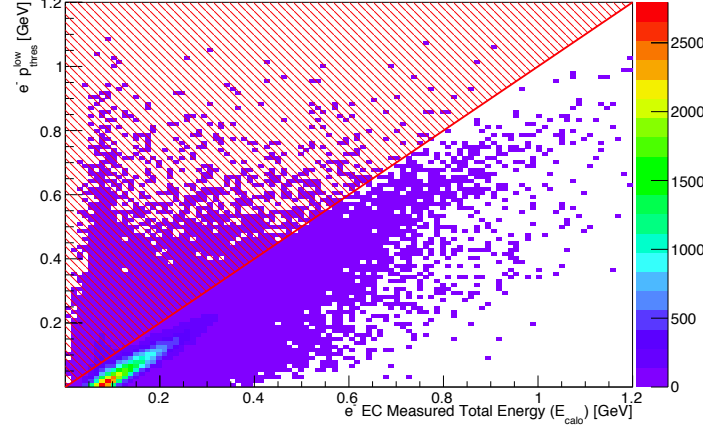


Figure 14: Plot of energy deposited measured by EC vs. track momentum $p_{\text{thres}}^{\text{low}}$ for electrons from π^0 events without the g12 lepton EC PID scheme applied. The red region depicts the cut that would reject events in the g12 lepton EC PID scheme. Image source: [44]

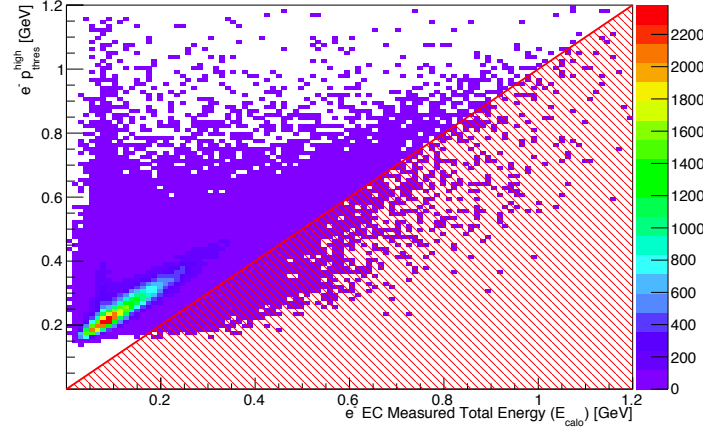


Figure 15: Plot of energy deposited measured by EC vs. track momentum $p_{\text{thres}}^{\text{high}}$ for electrons from π^0 events without the g12 lepton EC PID scheme applied. The red region depicts the cut that would reject events in the g12 lepton EC PID scheme. Image source: [44]

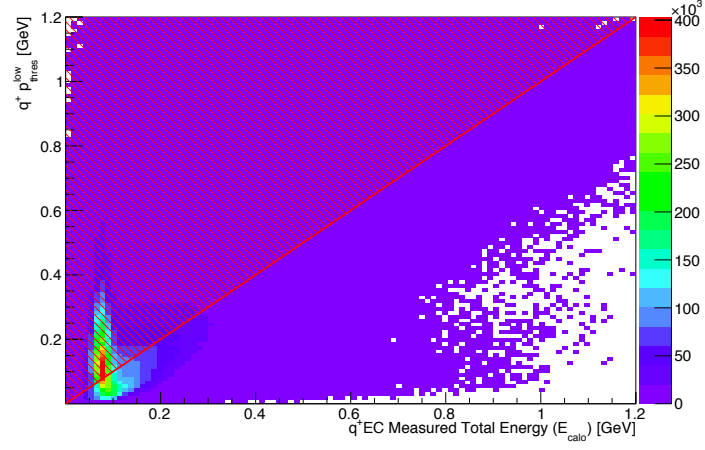


Figure 16: Plot of energy deposited measured by EC vs. track momentum $p_{\text{thres}}^{\text{low}}$ for positive charged tracks. The red region depicts the cut that would reject events in the g12 lepton EC PID scheme. Image source: [44]

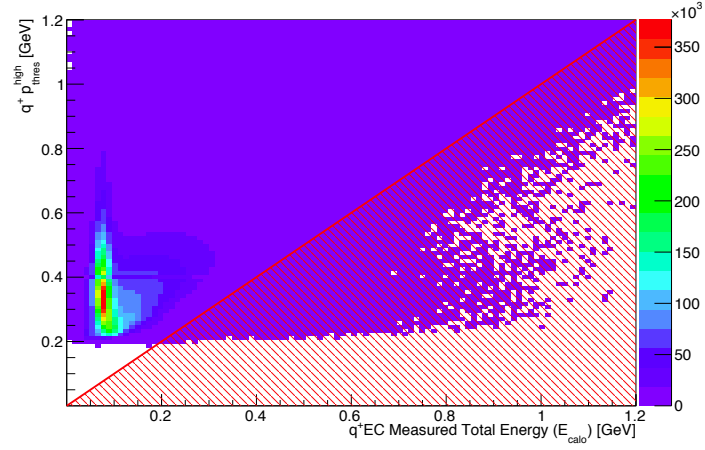


Figure 17: Plot of energy deposited measured by EC vs. track momentum $p_{\text{thres}}^{\text{high}}$ for positive charged tracks. The red region depicts the cut that would reject events in the g12 lepton EC PID scheme. Image source: [44]

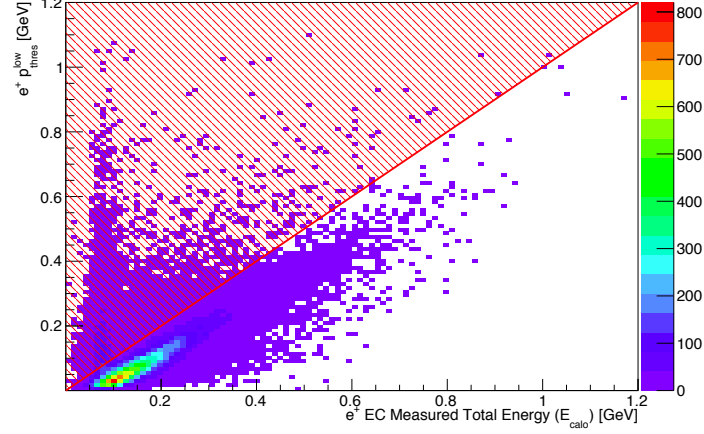


Figure 18: Plot of energy deposited measured by EC vs. track momentum $p_{\text{thres}}^{\text{low}}$ for positrons from π^0 events without the g12 lepton EC PID scheme applied. The red region depicts the cut that would reject events in the g12 lepton EC PID scheme. Image source: [44]

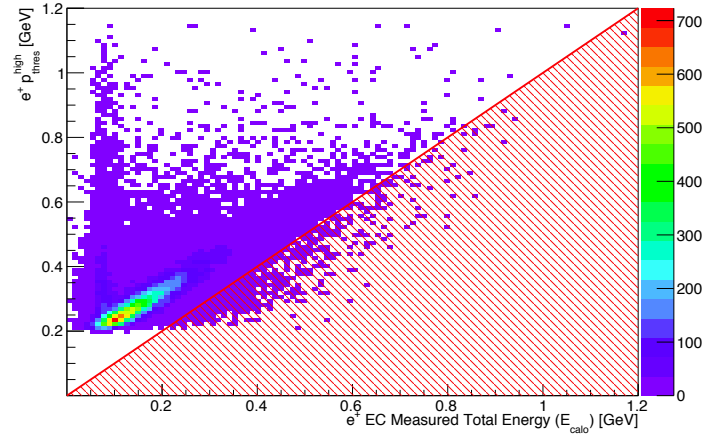


Figure 19: Plot of energy deposited measured by EC vs. track momentum $p_{\text{thres}}^{\text{high}}$ for positrons from π^0 events without the g12 lepton EC PID scheme applied. The red region depicts the cut that would reject events in the g12 lepton EC PID scheme. Image source: [44]

3.1.3 $\eta' \rightarrow e^+e^-\gamma$ with CLAS g12

The CLAS g12 vertex resolution was ≈ 10 mm (i.e. ten times larger than in the future CLAS12 apparatus) which was not suitable for a sufficient separation between external conversion and Dalitz events. However, the contamination from external conversion was only present in the low $M(e^+e^-)$ mass bins. [45]. Figure 20 shows the proton missing mass after reconstruction of $\eta' \rightarrow e^+e^-\gamma$ events in the CLAS g12 experiment.

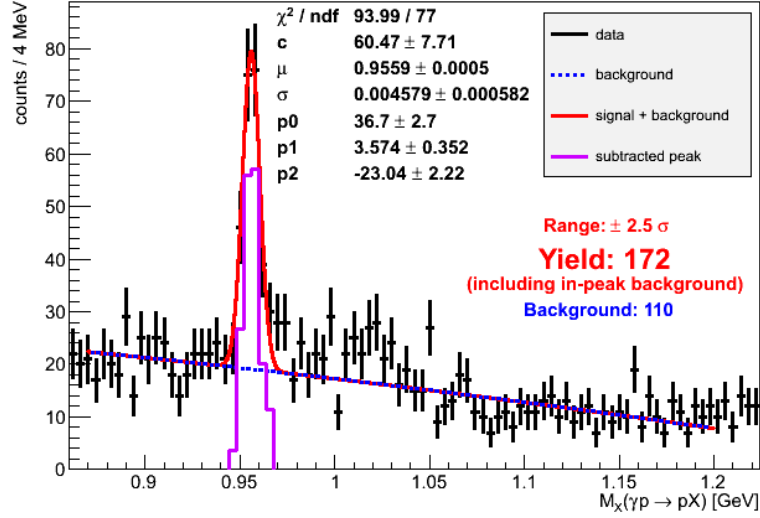


Figure 20: Missing mass of the proton for $\eta' \rightarrow e^+e^-\gamma$ from CLAS g12. [45] The signal is fitted by a gaussian function whereas the background is fitted by a third order polynomial (blue curve). The sum of both, signal and background, is indicated by the red curve.

The smooth background is related to Bethe-Heitler and time-like-Compton scattering, which could have been mitigated if the final stated photon from the Dalitz decay would be utilized. The predominant in-peak background contribution is related to the $\eta' \rightarrow \gamma\gamma$ decay. [45]. The missing mass spectrum in Fig. 20 shows the need for a high statistics sample in order to be able to perform a side-band subtraction for the dilepton invariant mass spectrum.

4 Measurement

This section is a description on how the $\eta \rightarrow e^+e^-\gamma$ was simulated and reconstructed for this CLAS12 proposal.

4.1 Simulation and Reconstruction

To simulate the reaction in Eq. 1, the program PLUTO++ [46] was utilized for its ability to simulate the decays of those according to QED, Vector Meson Dominance or a user defined TFF. For reconstruction of the desired topologies, the CLAS12 FASTMC [47] was used, in which $\sim 5 \cdot 10^8$ events were generated for $\eta' \rightarrow e^+e^-\gamma$ and then simulated with FASTMC at 75% torus field. The efficiency for all detectors are assumed to be 100% and only the geometric acceptance is considered for this proposal. Therefore the numbers that will be quoted in this proposal will be only an upper limit. An extra FASTMC simulation was performed for the torus field setting of 100% to show the effects of the magnetic field on the lepton acceptance.

The production of η' was weighted by photo-production differential cross-sections, $\frac{d\sigma}{d\Omega}(v, \cos\theta_{cm})$, published in [48], and Q^2 . Where v is the virtual photon energy, $\cos\theta_{cm}$ is the production angle in the center-of-mass frame of the system and Q^2 , the production virtual photon, is defined as $-(k - k')^2$. This was done to achieve a quasi realistic model of the production. The e^+e^- decay spectrum, of each meson, was weighted via the VMD model (including QED predictions). Another simulation was performed using a flat $M(e^+e^-)$ distribution (No QED, No VMD) to analyze any effects of the model on the e^+e^- acceptance. The analysis showed that the acceptance, in $M(e^+e^-)$, was independent of the decay model until $M(e^+e^-) \rightarrow M_{\eta'}$, see Fig.23.

4.1.1 Trigger Requirements

The standard CLAS12 electron trigger (HTCC(Nphe>2) * [(PCAL+EC)>1.0 GeV] is sufficient for this types of analysis. The rate for hadron production in electro-production where the scattered electron is left undetected is ~ 140 kHz [49]. This rate needs to be scaled down by the ratio of hadron production cross-section to η' production cross-section, see Eq. 13 in Sec. 4.2. This ratio was calculated $\sim \frac{1}{200}$, which leads to an overall rate of 0.7 kHz, while the expected data acquisition (DAQ) readout rate is 10 kHz.

4.1.2 Detection of e^+e^- Events

Electron/positron ID will include responses from the HTCC, PCAL and EC calorimeters. The energy information of the PCAL and the inner and outer parts of EC will be used to compare the total energy deposition with the momentum measured in the DC ($\alpha * (E_{Pcal} + E_{ECin} + E_{ECout}) \sim P_{DC}$), where α is a scaling factor.

4.1.3 Particle Identification

The η' meson have pion decay modes, which are orders of magnitude greater than the Dalitz decay. For example, the ratio $\Gamma_{\pi^+\pi^-\gamma}/\Gamma_{e^+e^-\gamma}$ is $6.2 \cdot 10^2$.

Electrons/positrons will be identified by using the information from the detectors described above. The expected e^\pm/π^\pm rejection factor for single particles ($p < 4.9$ GeV) is 10^3 for the HTCC, while the PCAL+EC can provide an additional factor of 10^2 . Combining both methods yields a e^\pm/π^\pm rejection factor of 10^5 which results in a $e^+e^-/\pi^+\pi^-$ rejection factor of 10^{10} . Therefore, the amount of $\pi^+\pi^-$ background in the $M(e^+e^-)$ spectrum will be $\approx 6.2 \cdot 10^2/10^{10} = 6.2 \cdot 10^{-8}$. A detailed explanation of particle identification for e^+e^- pairs can be found in [50].

4.1.4 Acceptance

An inclusive reconstruction scheme

$$ep \rightarrow e'p\eta' \rightarrow pe^+\gamma e^-(e^-) \quad (12)$$

where a proton, a photon, a positron and one electron of unknown source is detected. It will be determined from kinematics which electron corresponds to: (a) beam scattered electron or (b) the Dalitz produced electron. In Fig. 21 below the inference of choosing the missing e^- according to kinematics is shown. It is clearly shown that the combinatorial background from choosing the incorrect e^- is manageable.

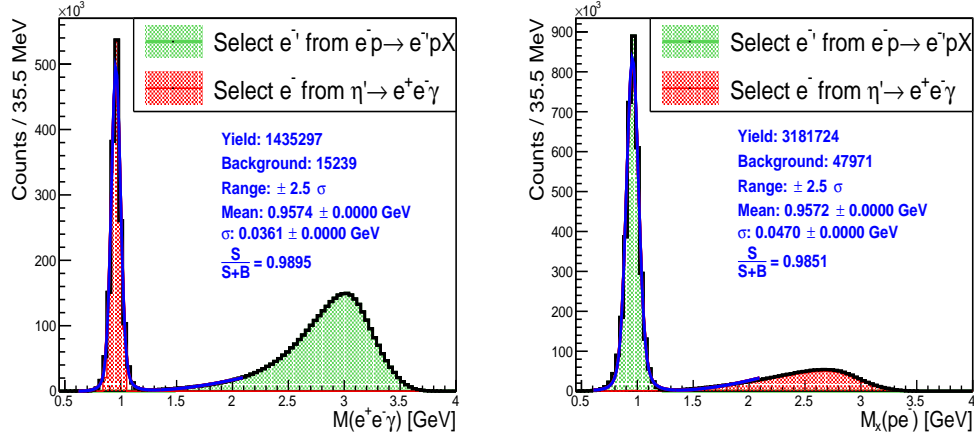


Figure 21: (Left) Invariant mass of $e^+e^-\gamma$. (Right) Missing mass off of the proton and one e^- . Red corresponds to the Dalitz e^- being detected and selected, while green is when the scattered beam e^- is detected and rejected. Blue line is a fit using a Voigtian + 2nd order polynomial.

After placing a cut of 2.5σ from the mean value of the fit for the left diagram in Fig. 21, we conclude from Fig. 22 that the background from leakage of the incorrect e^- is negligible.

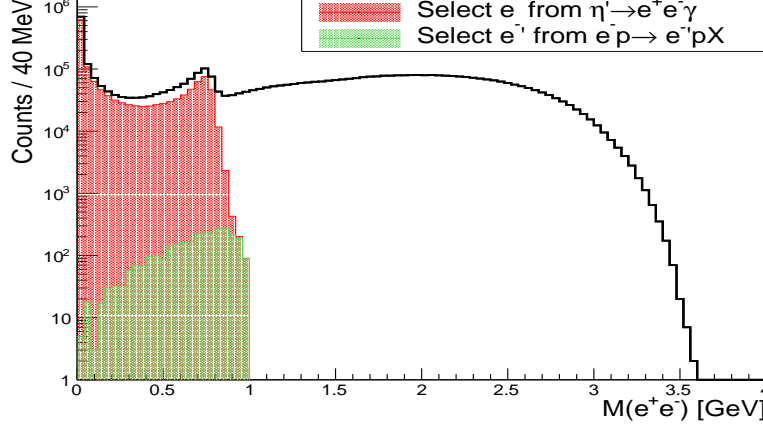


Figure 22: Invariant mass of e^+e^- . Red corresponds to the Dalitz e^- being detected and selected, while green is when the scattered beam e^- is detected but accepted in the kinematics.

The acceptance was calculated by dividing the accepted events by the generated events, per $M(e^+e^-)$ bin. The η' Dalitz decay acceptance using the VMD model along with the acceptance using a flat e^+e^- mass distribution can be seen in Fig.23.

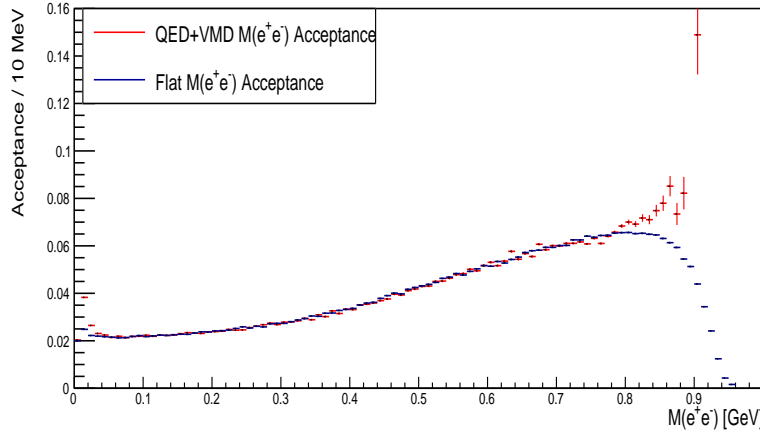


Figure 23: (Color Online) Acceptance as a function of $M(e^+e^-)$ using two decay models.

4.2 Calculating the Expected Yield

The expected yield for $ep \rightarrow e'p\eta'[\eta' \rightarrow pe^+e^-\gamma]$ is calculated under the assumption, that the η' electro-production cross-section can be deduced from the η' photo-production cross-section. A qualitative justification of this assumption may be found in Fig. 24. The shape of the cross-section distributions for $ep \rightarrow e'p\eta$, shown in the top row of Fig. 24, are comparable to the corresponding distribution for $\gamma p \rightarrow p\eta$, plotted in the bottom row of Fig. 24. The major difference is related to the scaling rule of $1/Q^2$, i.e. the electro-production cross-section might be approximated by the photo-production cross-section by scaling down the latter one by $1/Q^2$.

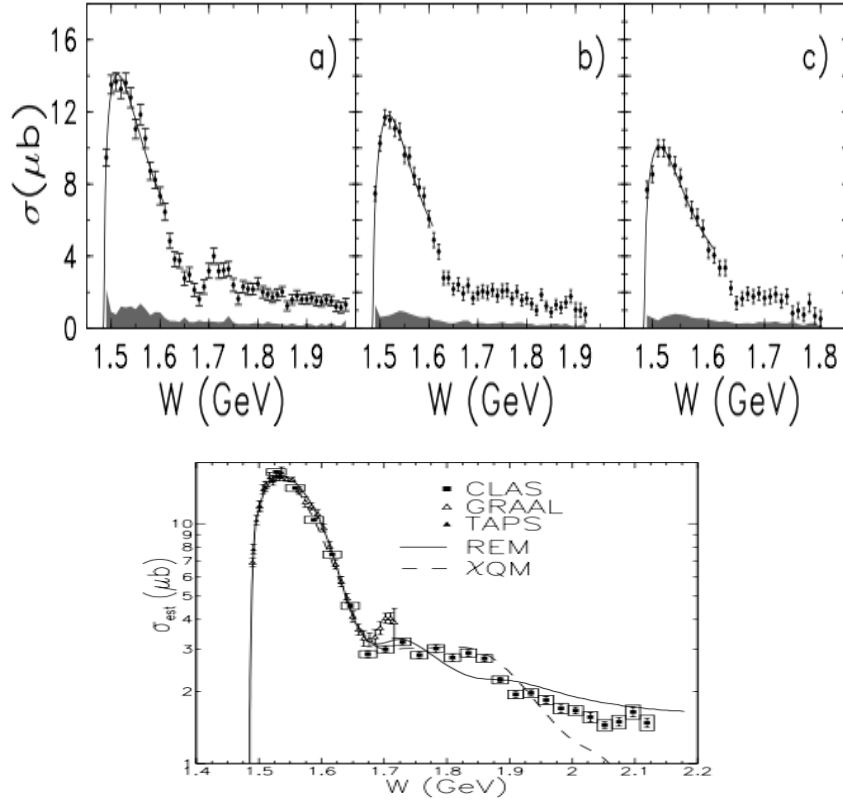


Figure 24: Integrated cross-section for $ep \rightarrow e'p\eta$ (Top) for: (a) $Q^2 = 0.625(\text{GeV}/c)^2$, (b) $Q^2 = 0.875(\text{GeV}/c)^2$, (c) $Q^2 = 1.125(\text{GeV}/c)^2$ [51] and for $\gamma p \rightarrow p\eta$ (Bottom) [52].

The top row of Fig. 25 shows the total photo-production cross-section for hadrons in comparison with the photo-production cross-section for η' (see bottom row of Fig. 25). Due to the considerations made above, these two cross-section distributions might be directly translated to the corresponding

electro-production cross-sections. Using the distributions shown in Fig. 25, one might define the following ratio $R(W)$:

$$R(W) = \frac{\sigma(W)}{\eta' \text{ integrated } \sigma(W)} \quad (13)$$

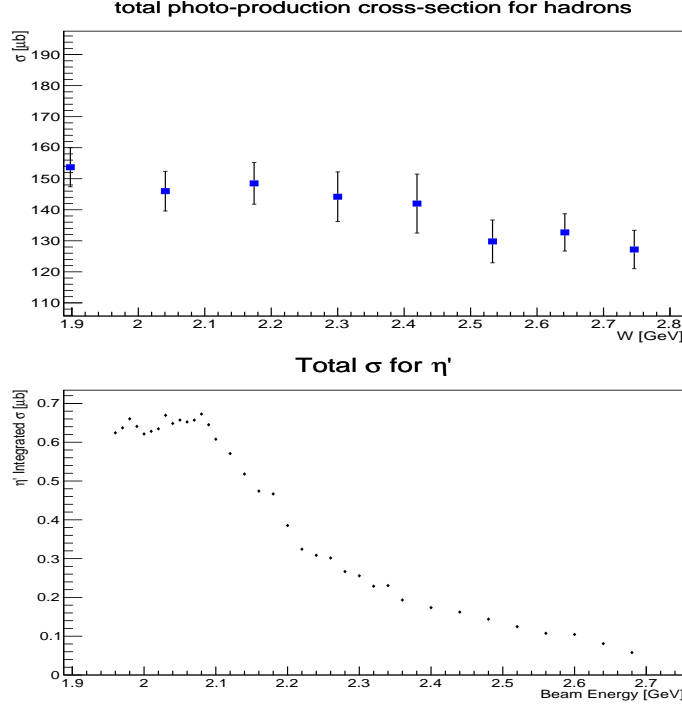


Figure 25: Integrated cross-section for $\gamma p \rightarrow pX$ (Top) and $\gamma p \rightarrow p\eta'$ (Bottom) as a function of W .

The rate for mesons in electro-production where the scattered electron is left undetected is ~ 140 kHz [49]. This rate needs to be scaled down by $R(W)$ in order to achieve the corresponding rate for η' production. This leads to:

$$\eta' \text{ total rates} / 80 \text{ Days } (W) = 140 \text{ kHz} \cdot \frac{86,400 \text{ seconds}}{80 \text{ days}} \cdot \frac{1}{R(W)} \quad (14)$$

A plot of Eq. 14 is shown in Fig. 26 (left y-axis). The total $\eta' \rightarrow e^+e^-\gamma$ rates per 80 days, and as a function W , is calculated by multiplying Eq.14 with the product of the average detection efficiency $\epsilon \approx 5\%$ as well as the branching fraction $\mathcal{BR} = 4.69 \cdot 10^{-4}$ [31] for $\eta' \rightarrow e^+e^-\gamma$. The corresponding plot is shown in Fig. 26 (right y-axis). The total number N_{tot} of expected

$\eta' \rightarrow e^+e^-\gamma$ events after 80 days of measurement is given by the integral of Fig. 26 over W . This leads to the expected yield:

$$N_{tot} = \int_{1.9 \text{ GeV}}^{2.8 \text{ GeV}} \left[N(W)_{\eta' \rightarrow e^+e^-\gamma} / 80 \text{ Days} \right] dW = \frac{52,100 \text{ events}}{80 \text{ Days}} \quad (15)$$

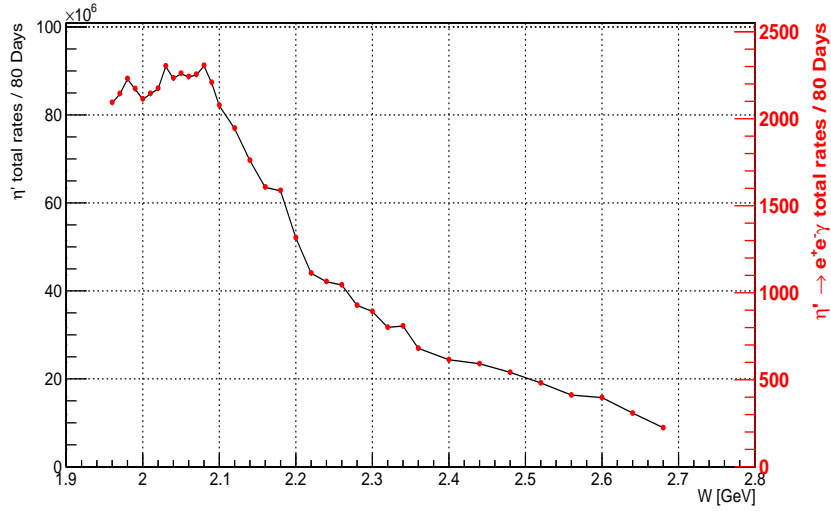


Figure 26: Total η' production rate per 80 days (left y-axis) and total $\eta' \rightarrow e^+e^-\gamma$ rates per 80 days (right y-axis) as a function of W . Both rates have been calculated according to Eq. 14

Instead of using an average efficiency $\epsilon \sim 5\%$ for determining the expected yield, one could utilize the $M(e^+e^-)$ dependent acceptance shown in Fig. 23 to calculate the total expected yield using the same procedure as explained above. This number of events expected to be reconstructed as well as the acceptance corrected yield can be seen in Fig. 27 which is consistent with the previous number quoted in Eq. 15.

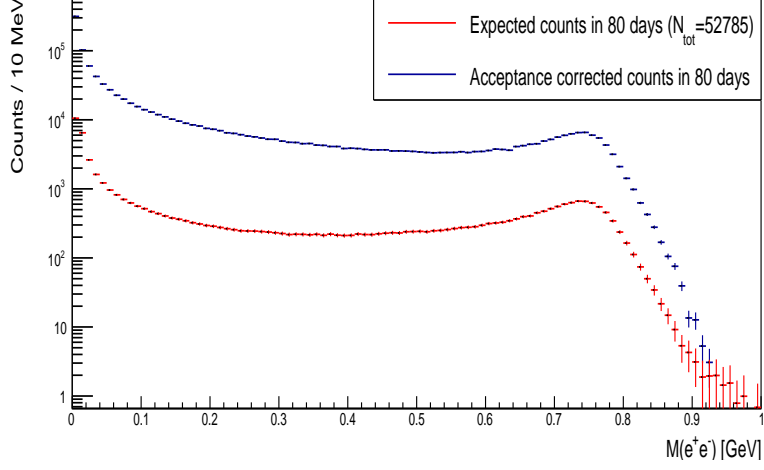


Figure 27: (Color Online) Expected yield as a function of $M(e^+e^-)$.

From Fig. 27 the QED normalized spectrum can be deduced and is shown in Fig. 28. Both acceptance models (i.e. flat and QED+VMD) are used to determine the transition form factor. It is shown that there exists a systematic uncertainty depending on the chosen acceptance model. However, the final calculation on the slope parameter or the TFF shows a negligible impact of this uncertainty. Regardless of the acceptance model, it is shown in Fig. 28 that the accumulated statistics collected by CLAS12 allow for a precision of each parameter $\lesssim 0.5\%$.

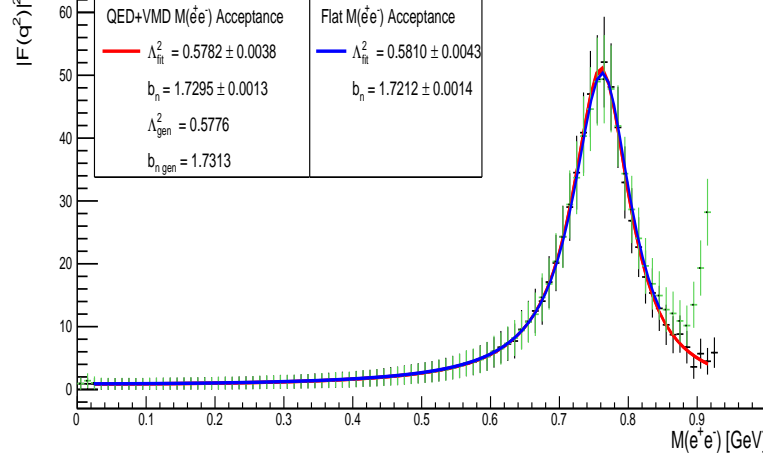


Figure 28: (Color Online) $|F(q^2)|^2$ as a function of $M(e^+e^-)$ using two acceptance models. (black points) QED+VMD $M(e^+e^-)$ acceptance model. (green points) Flat $M(e^+e^-)$ acceptance model. The solid lines represent a fit using Eq. 8 to the data points.

4.3 Acceptance at 100% Torus field

An addition simulation was performed using the same generated data shown above, the difference being the setting of the torus magnetic field. Below, in Fig. 29, the ratio of the lepton acceptance for the two different torus settings is depicted.

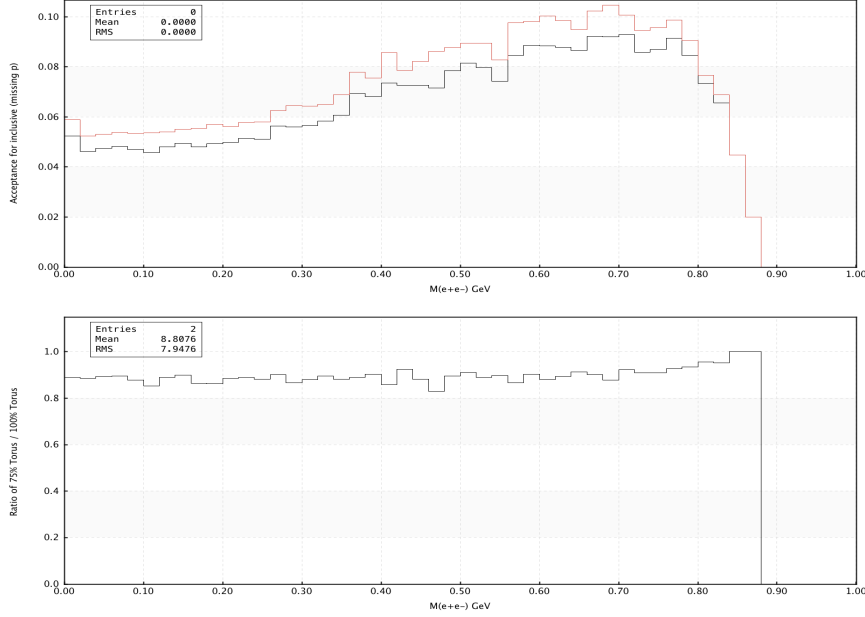


Figure 29: Acceptance using a VMD decay model, as a function of $M(e^+e^-)$ for the inclusive scheme(Top). The torus field was set to 75%(red) as well as 100%(black). Ratio of the acceptances plotted above (75%/100%)(Bottom).

4.4 Expected Systematic Uncertainties

The major sources of systematic uncertainties are the acceptance and particle identification. The lepton acceptance uncertainty is estimated to be $\lesssim 5\%$ which was observed in former CLAS experiments. The lepton identification uncertainty will arise from the performance of the HTCC, PCAL and EC. From simulation studies performed for this proposal, all leptons and final state photons are detected within the geometric space of the PCAL+EC with hit coincidences in both. Furthermore, all leptons, within a few percent, that were detected in the PCAL+EC were also detected in the HTCC. Further systematics from pion contamination are mitigated by the pion rejection factor described above. Systematics related to external photon conversion are minimal due to the 1 mm resolution of the primary vertex given by the Silicon Vertex Tracker (SVT) as shown in Sec 2.3. Any Bethe-Heitler contributions are negligible when utilizing an exclusive meson reconstruction scheme.

5 Beam Time Request

With this proposal and beam time request, we ask for 100 days of beam time. Of the 100 days, 80 days will be dedicated to the production beam time with the standard CLAS setup, at full luminosity ($\sim 10^{35}\text{cm}^{-2}\text{s}^{-1}$) with 75% torus field. The remaining 20 days will be dedicated to optimizing and testing the trigger set-up (HTCC + PCAL + EC). This request should provide a competitive data sample of $\eta' \rightarrow e^+e^-\gamma$. The CLAS12 configuration we propose for the measurement of the transition form factors is compatible with the experimental setup already established by Run Group A.

References

- [1] Fred Jegerlehner and Andreas Nyffeler. The Muon $g-2$. *Phys. Rept.*, 477:1–110, 2009.
- [2] Thomas Blum, Achim Denig, Ivan Logashenko, Eduardo de Rafael, B. Lee Roberts, Thomas Teubner, and Graziano Venanzoni. The Muon $(g-2)$ Theory Value: Present and Future. 2013.
- [3] J.P. Miller et al. Muon $(g-2)$: experiment and theory. *Reports on Progress in Physics*, 70(5):795, 2007.
- [4] G. W. Bennett et al. Final Report of the Muon E821 Anomalous Magnetic Moment Measurement at BNL. *Phys. Rev.*, D73:072003, 2006.
- [5] Michel Davier, Andreas Hoecker, Bogdan Malaescu, and Zhiqing Zhang. Reevaluation of the Hadronic Contributions to the Muon $g-2$ and to $\alpha(M_Z)$. *Eur. Phys. J.*, C71:1515, 2011. [Erratum: *Eur. Phys. J.* C72,1874(2012)].
- [6] Kaoru Hagiwara, Ruofan Liao, Alan D. Martin, Daisuke Nomura, and Thomas Teubner. $(g-2)_{\mu}$ and $\alpha(M_Z^2)$ re-evaluated using new precise data. *J. Phys.*, G38:085003, 2011.
- [7] J. Grange et al. Muon $(g-2)$ Technical Design Report. 2015.
- [8] Naohito Saito. A novel precision measurement of muon $g-2$ and EDM at J-PARC. *AIP Conf. Proc.*, 1467:45–56, 2012.
- [9] Johan Bijnens and Joaquim Prades. The Hadronic Light-by-Light Contribution to the Muon Anomalous Magnetic Moment: Where do we stand? *Mod. Phys. Lett.*, A22:767–782, 2007.
- [10] Christof Gattringer and Christian B. Lang. Quantum chromodynamics on the lattice. *Lect. Notes Phys.*, 788:1–343, 2010.
- [11] Thomas Blum, Saumitra Chowdhury, Masashi Hayakawa, and Taku Izubuchi. Hadronic light-by-light scattering contribution to the muon anomalous magnetic moment from lattice QCD. *Phys. Rev. Lett.*, 114(1):012001, 2015.
- [12] Gilberto Colangelo, Martin Hoferichter, Massimiliano Procura, and Peter Stoffer. Dispersive approach to hadronic light-by-light scattering. *JHEP*, 09:091, 2014.
- [13] Vladyslav Pauk and Marc Vanderhaeghen. Anomalous magnetic moment of the muon in a dispersive approach. *Phys. Rev.*, D90(11):113012, 2014.

- [14] Gilberto Colangelo, Martin Hoferichter, Bastian Kubis, Massimiliano Procura, and Peter Stoffer. Towards a data-driven analysis of hadronic light-by-light scattering. *Phys. Lett.*, B738:6–12, 2014.
- [15] Gilberto Colangelo, Martin Hoferichter, Massimiliano Procura, and Peter Stoffer. Dispersion relation for hadronic light-by-light scattering: theoretical foundations. *JHEP*, 09:074, 2015.
- [16] P. Adlarson et al. Exclusive Measurement of the $\eta \rightarrow \pi^+\pi^-\gamma$ Decay. *Phys. Lett.*, B707:243–249, 2012.
- [17] F. Stollenwerk, C. Hanhart, A. Kupsc, U. G. Meissner, and A. Wirzba. Model-independent approach to $\eta \rightarrow \pi^+\pi^-\gamma$ and $\eta' \rightarrow \pi^+\pi^-\gamma$. *Phys. Lett.*, B707:184–190, 2012.
- [18] C. Hanhart, A. Kupsc, U. G. Meißner, F. Stollenwerk, and A. Wirzba. Dispersive analysis for $\eta \rightarrow \gamma\gamma^*$. *Eur. Phys. J.*, C73(12):2668, 2013. [Erratum: *Eur. Phys. J.*C75,no.6,242(2015)].
- [19] Bastian Kubis and Judith Plenter. Anomalous decay and scattering processes of the η meson. *Eur. Phys. J.*, C75(6):283, 2015.
- [20] C. W. Xiao, T. Dato, C. Hanhart, B. Kubis, U. G. Meißner, and A. Wirzba. Towards an improved understanding of $\eta \rightarrow \gamma\gamma^*$. 2015.
- [21] A. Nyffeler. On the precision of a data-driven estimate of hadronic light-by-light scattering in the muon g-2: pseudoscalar-pole contribution. *arXiv*, (1602.03398), 2016.
- [22] R H Dalitz. On an alternative decay process for the neutral π^0 -meson. *Proceedings of the Physical Society. Section A*, 64(7):667, 1951.
- [23] J. J. Lord, Joseph Fainberg, D. fas. Haskin, and Marcel Schein. Narrow angle pairs of particles from nuclear interactions. *Phys. Rev.*, 87:538–539, Aug 1952.
- [24] N. P. Samios. Dynamics of internally converted electron-positron pairs. *Phys. Rev.*, 121:275–281, Jan 1961.
- [25] P. Lindenfeld, A. Sachs, and J. Steinberger. The Internal Pair Production of γ -Rays of Mesonic Origin; Alternate Modes of π^0 Decay. *Physical Review*, 89:531–537, February 1953.
- [26] C. P. Sargent, R. Cornelius, M. Rinehart, L. M. Lederman, and K. Rogers. Diffusion cloud-chamber study of very slow mesons. i. internal pair formation. *Phys. Rev.*, 98:1349–1354, Jun 1955.

- [27] Norman M. Kroll and Walter Wada. Internal pair production associated with the emission of high-energy gamma rays. *Phys. Rev.*, 98:1355–1359, Jun 1955.
- [28] P. Stoler et al. Hard exclusive electroproduction of pi0 and eta with clas12. Technical report, **CLAS Analysis Proposal E12-06-108**, 2011.
- [29] P. Stoler et al. Exclusive phi meson electroproduction with clas12. Technical report, **CLAS Analysis Proposal E12-12-007**, 2012.
- [30] L.G. Landsberg. Electromagnetic decays of light mesons. *Physics Reports*, 128(6):301 – 376, 1985.
- [31] M. Ablikim and et. al. Observation of the dalitz decay $\eta' \rightarrow \gamma e^+ e^-$. *Phys. Rev. D*, 92:012001, Jul 2015.
- [32] M.C. Kunkel. Light Meson Decays in CLAS.
- [33] F. Farzanpay et al. Measurement of the slope of the π^0 electromagnetic form factor. *Physics Letters B*, 278(4):413 – 418, 1992.
- [34] H. Berghäuser et al. Determination of the η -transition form factor in the reaction. *Physics Letters B*, 701(5):562 – 567, 2011.
- [35] P. Aguar-Bartolomé and others. New determination of the η transition form factor in the dalitz decay $\eta' \rightarrow e^+ e^- \gamma$ with the crystal ball/taps detectors at the mainz microtron. *Phys. Rev. C*, 89:044608, Apr 2014.
- [36] R. I. Dzhelyadin et al. Study of the Electromagnetic Transition Form-factor in $\omega \rightarrow \pi^0 \mu^+ \mu^-$ Decay. *Phys. Lett.*, B102:296, 1981. [JETP Lett.33,228(1981)].
- [37] R. Arnaldi et al. Study of the electromagnetic transition form-factors in eta \rightarrow mu+ mu- gamma and omega \rightarrow mu+ mu- pi0 decays with NA60. *Phys. Lett.*, B677:260–266, 2009.
- [38] Antonio Uras. Measurement of the η and ω Dalitz decays transition form factors in p-A collisions at 400 GeV/c with the NA60 apparatus. *J. Phys. Conf. Ser.*, 270:012038, 2011.
- [39] R. Briere and others (CLEO Collaboration). Rare decays of the η' . 1999.
- [40] R.I. Dzhelyadin and others. Observation of $\eta' \rightarrow \mu^+ \mu^- \gamma$ decay. *Physics Letters B*, 88(3):379 – 380, 1979.
- [41] M. Ablikim et al. Observation of the Dalitz Decay $\eta' \rightarrow \gamma e^+ e^-$. *Phys. Rev.*, D92(1):012001, 2015.

- [42] D. Babusci et al. Study of the Dalitz decay $\phi \rightarrow \eta e^+ e^-$ with the KLOE detector. *Phys. Lett.*, B742:1–6, 2015.
- [43] Z. Akbar et al. g12 Analysis Procedures, Statistics and Systematics. Technical report, CLAS Technical Note, 2016.
- [44] M.C. Kunkel. *Photoproduction of π^0 on hydrogen with CLAS from 1.1 GeV - 5.45 GeV using $e^+e^-\gamma$ decay*. PhD thesis, Old Dominion University, 2014.
- [45] M. Schever. Towards Measuring the Electromagnetic Structure of η' Mesons with CLAS , 2015.
- [46] I. Frohlich, I. Froehlich, Lorenzo Cazon, T. Galatyuk, V. Hejny, et al. Pluto: A Monte Carlo Simulation Tool for Hadronic Physics. *PoS, ACAT2007:076*, 2007.
- [47] CLAS software repository. Monte-carlo program to simulate clas12 detector response. Technical report, 2016.
- [48] M. Williams et al. Differential cross sections for the reactions $\gamma p \rightarrow p\eta$ and $\gamma p \rightarrow p\eta'$. *Phys. Rev. C*, 80:045213, Oct 2009.
- [49] M. Sargsyan et al. CLAS-NOTE 90-007. Technical report, CLAS Technical Note, 1990.
- [50] P. Nadel-Turonski et al. Timelike Compton Scattering and J/ψ photoproduction on the proton in e^+e^- pair production with CLAS12 at 11 GeV. Technical report, CLAS Analysis Proposal E12-12-001, 2012.
- [51] R. Thompson et al. The $ep \rightarrow e' p\eta$ reaction at and above the $s_{11}(1535)$ baryon resonance. *Phys. Rev. Lett.*, 86:1702–1706, Feb 2001.
- [52] M. Dugger et al. η photoproduction on the proton for photon energies from 0.75 to 1.95 gev. *Phys. Rev. Lett.*, 89:222002, Nov 2002.
- [53] M.E. Peskin and D.V. Schroeder. *An Introduction to Quantum Field Theory*. Advanced book classics. Addison-Wesley Publishing Company, 1995.
- [54] F. Halzen and A.D. Martin. *Quarks and leptons: an introductory course in modern particle physics*. Wiley, 1984.
- [55] K.A. Olive et al. Review of particle physics. *Phys. Rev. C*, 38:090001, 2014.

Appendices

A Decay Kinematics

A.1 $\eta' \rightarrow \gamma\gamma$ Decay

As shown in Fig. 2a, the two photon decay can be expressed in terms of the respective momentum, $P_p(\eta') \rightarrow \gamma(\epsilon_1, p)\gamma(\epsilon_2, k)$, where ϵ_1 and ϵ_2 are the polarizations of the photons with 4-momenta p and k . Dropping the nomenclature (η') in $P_p(\eta')$, the four momentum of the decaying meson is $P_p = p + k$. Using the Feynman rules as given in [53] and [54], which are Lorentz and gauge invariant and also parity conserving, the amplitude can be solved to be:

$$\mathcal{M}(P_P \rightarrow \gamma(\epsilon_1, p)\gamma(\epsilon_2, k)) = M_P(p^2 = 0, k^2 = 0)\varepsilon_{\mu\nu\rho\sigma}\epsilon_1^\mu p^\nu \epsilon_2^\rho k^\sigma \quad (16)$$

where $\varepsilon_{\mu\nu\rho\sigma}$ is the antisymmetric metric tensor. The form factor, $M_P(p^2 = 0, k^2 = 0)$, contains information of the decaying meson and since the decay products are on-shell photons, which are massless, M_P is a constant given as;

$$M_P = \begin{cases} \frac{\alpha}{\pi f_\pi} & \text{if } P = \pi^0; \\ \frac{\alpha}{\pi f_\pi} \frac{1}{\sqrt{3}} \left(\frac{f_\pi}{f_8} \cos \theta_{mix} - 2\sqrt{2} \frac{f_\pi}{f_0} \sin \theta_{mix} \right) & \text{if } P = \eta; \\ \frac{\alpha}{\pi f_\pi} \frac{1}{\sqrt{3}} \left(\frac{f_\pi}{f_8} \sin \theta_{mix} + 2\sqrt{2} \frac{f_\pi}{f_0} \cos \theta_{mix} \right) & \text{if } P = \eta' \end{cases} \quad (17)$$

where $\alpha = e^2/4\pi \approx 1/137$ is the fine structure constant, $f_\pi \approx 92.4 \text{ MeV}$ is the physical value of the pion-decay constant and $f_0 \approx 1.04 f_\pi$ and $f_8 \approx 1.3 f_\pi$ are the singlet and octet Pseudo-Goldstone meson decay constants.

A.1.1 Squared Matrix Element

The squared matrix element of the decay $P_P \rightarrow \gamma(\epsilon_1, p)\gamma(\epsilon_2, k)$ is given by

$$|\mathcal{M}(P_P \rightarrow \gamma(\epsilon_1, p)\gamma(\epsilon_2, k))|^2 = |M_P|^2 \varepsilon_{\mu\nu\rho\sigma} \varepsilon_{\mu'\nu'\rho'\sigma'} \epsilon_1^\mu p^\nu \epsilon_2^\rho k^\sigma \epsilon_1^{\mu'} p^{\nu'} \epsilon_2^{\rho'} k^{\sigma'} \quad (18)$$

which can be simplified to;

$$|\mathcal{M}(P_P \rightarrow \gamma(p)\gamma(k))|^2 = |M_P|^2 \varepsilon_{\mu\nu\rho\sigma} \varepsilon^{\mu\nu}_{\rho'\sigma'} p^\rho p^{\rho'} k^\sigma k^{\sigma'} \quad (19)$$

by assuming that the polarizations of the photons remain unobserved, as they are in CLAS. Therefore the photon polarization vectors can be summed

using Eq. 5.75 from [53] which reads as;

$$\sum_{\text{polarizations}} \epsilon_\mu \epsilon_{\mu'} \rightarrow -g_{\mu\mu'} \quad (20)$$

As indicated in [53], the right arrow indicates that this is not an actual equality, but the solution is valid as long as both sides are dotted into Eq. 18. The antisymmetric tensor, $\epsilon_{\mu\nu\rho\sigma} \epsilon^{\mu\nu}_{\rho'\sigma'}$ is simplified using Eq. A.30 of [53];

$$\epsilon_{\mu\nu\rho\sigma} \epsilon^{\mu\nu}_{\rho'\sigma'} = -2(g_{\rho\rho'} g_{\sigma\sigma'} - g_{\rho\sigma'} g_{\rho'\sigma}) \quad (21)$$

Applying Eq. 21 to Eq. 19 results in;

$$|\mathcal{M}(P_P \rightarrow \gamma(p)\gamma(k))|^2 = |M_P|^2 (-2)(p^2 k^2 - (p \cdot k)^2) . \quad (22)$$

Substituting

$$(p+k)^2 = p^2 + k^2 + 2(p \cdot k) , \quad (23)$$

and applying $p^2 = k^2 = 0$, since both photons are massless because they are on-shell, we can derive the final expression of the squared amplitude of the decay $P_P \rightarrow \gamma(\epsilon_1, p)\gamma(\epsilon_2, k)$ as;

$$|\mathcal{M}(P_P \rightarrow \gamma(p)\gamma(k))|^2 = |M_P|^2 \frac{1}{2}(p+k)^4 = \frac{1}{2} |M_P|^2 m_P^4 \quad (24)$$

where m_P^4 is the mass of the η' derived from the 4-momenta conservation equation $(p+k)^4 = m_P^4$

A.1.2 Decay rate

The decay rate of a two-body decay is explained in Equation 46.17 of [55] as

$$d\Gamma = \frac{1}{32\pi^2} A |\mathcal{M}|^2 \frac{|\mathbf{p}_1|}{m_p^2} d\Omega , \quad (25)$$

where $d\Omega$ is the solid angle of particle 1 and A is the symmetry factor which appears because of the Bose symmetry of the two outgoing photons. Substituting the square matrix element from Eq. 24 into Eq. 25 and integrating over the solid angle yields;

$$\Gamma_{P \rightarrow \gamma\gamma} = \frac{1}{32\pi^2} \frac{1}{2} |\mathcal{M}(P_P \rightarrow \gamma(p)\gamma(k))|^2 \frac{|\mathbf{p}|}{m_P^2} 4\pi = \frac{1}{32\pi} |M_P|^2 m_P^2 |\mathbf{p}| \quad (26)$$

Finally, in the center-of-mass (C.M.) frame of the decaying meson, $\mathbf{p} = \mathbf{E}_\gamma^{\text{C.M.}} = \frac{m_P}{2}$, we find the final expression of the decay rate of $P_P \rightarrow \gamma(\epsilon_1, p)\gamma(\epsilon_2, k)$ as;

$$\Gamma_{P \rightarrow \gamma\gamma} = \frac{1}{64\pi} |M_P|^2 m_P^3 . \quad (27)$$

A.2 η' Dalitz Decay

When a pseudoscalar meson decays via a photon γ and a dilepton (l^+l^-) pair, it is known as a Dalitz decay or a so-called single off-shell decay. The Dalitz decay is related to the two photon decay. However, in the Dalitz decay, one of the photons is off-shell (γ^*) and decays into a dilepton pair. Since the Dalitz decay is related to the two photon decay, the form factor of the Dalitz decay, for $P(\eta')$, will be similar to the form factor of the two photon decay of $P(\eta')$, except there will be an effective mass dependence for the Dalitz decay. Figure 2b depicts the Feymann diagram of the Dalitz decay.

The amplitude for the decay $P_P \rightarrow \gamma^*(p)\gamma(k) \rightarrow l^+(p_+)l^-(p_-)\gamma(k)$ is given by the following expression:

$$\mathcal{M}(P \rightarrow l^+(p_+, s_+)l^-(p_-, s_-)\gamma) = M_P(p^2, k^2 = 0)\varepsilon_{\mu\nu\rho\sigma}\frac{1}{q^2} \times [e\bar{u}(p_-, s_-)\gamma^\mu v(p_+, s_-)q^\nu \epsilon^\rho k^\sigma]. \quad (28)$$

Comparing the amplitudes of Eq. 28 and Eq. 16 it is seen that the polarization of the off-shell photon turned into the current $e\bar{u}(p_-, s_-)\gamma^\mu v(p_+, s_-)$ of the lepton pair. The parameters s_\pm are the spin helicities of the outgoing leptons l^\pm and as in Eq. 18, ϵ is the polarization of the outgoing photon.

A.2.1 Squared Matrix Element

$$|\mathcal{M}(P \rightarrow l^+(p_+, s_+)l^-(p_-, s_-)\gamma)|^2 = \frac{e^2}{(q^2)^2} |M|^2 \varepsilon_{\mu\nu\rho\sigma}\varepsilon_{\mu'\nu'\rho'\sigma'} \times [\bar{u}(p_-, s_-)\gamma^\mu v(p_+, s_+)\bar{v}(p_+, s_+)\gamma^{\mu'} u(p_-, s_-)q^\nu \epsilon^\rho k^\sigma q^{\nu'} \epsilon^{\rho'} k^{\sigma'}]. \quad (29)$$

using an equation found between equation 5.3 and 5.4 found in [53]

$$\begin{aligned} \sum_{s_-, s_+} \bar{u}(p_-, s_-)\gamma^\mu v(p_+, s_+)\bar{v}(p_+, s_+)\gamma^{\mu'} u(p_-, s_-) &= Tr[(\not{p}_- + m)\gamma^\mu(\not{p}_+ - m)\gamma^{\mu'}] \\ &= 2q^2 \left[-(g_{\mu\mu'} - \frac{p_\mu p_{\mu'}}{q^2}) - \frac{(p_+ - p_-)_\mu (p_+ - p_-)_{\mu'}}{q^2} \right] \end{aligned} \quad (30)$$

where the identity $q = p_+ + p_-$ was used. Substituting Eq. 30 into Eq. 29

$$|\mathcal{M}|^2 = \frac{2e^2 |M_P|^2}{q^2} \varepsilon_{\mu\nu\rho\sigma}\varepsilon_{\mu'\nu'\rho'\sigma'} \left[-g^{\mu\mu'} - \frac{(p_+ - p_-)^\mu (p_+ - p_-)^{\mu'}}{q^2} \right] \times [(-g^{\nu\nu'})q^\rho k^\sigma q^{\rho'} k^{\sigma'}] \quad (31)$$

Substituting $k = P - q$ and $p_- = q - p_+$ into Eq. 31

$$|\mathcal{M}|^2 = \frac{2e^2 |M_P|^2}{q^2} \varepsilon_{\mu\nu\rho\sigma} \varepsilon_{\mu'\nu'\rho'\sigma'} \left[-g^{\mu\mu'} - \frac{(2p_+ - q)^\mu (2p_+ - q)^{\mu'}}{q^2} \right] \times \\ (-g^{\nu\nu'}) (q^\rho P^\sigma - q^\rho q^\sigma) (q^{\rho'} P^{\sigma'} - q^{\rho'} q^{\sigma'}) \quad (32)$$

Applying properties of $-g^{\mu\mu'}$ and $-g^{\nu\nu'}$ onto Eq. 32

$$|\mathcal{M}|^2 = \frac{2e^2 |M_P|^2}{q^2} \left[\varepsilon_{\mu\nu\rho\sigma} \varepsilon^{\mu\nu}_{\rho'\sigma'} q^\rho P^\sigma q^{\rho'} P^{\sigma'} + \right. \\ \left. \frac{4}{q^2} \varepsilon_{\mu\nu\rho\sigma} \varepsilon^\mu_{\nu'\rho'\sigma'} p_+^\nu p_+^{\nu'} q^\rho q^{\rho'} P^\sigma P^{\sigma'} \right] \quad (33)$$

Switching to the rest frame of the pseudoscalar meson, P_p , the 4-momenta is transformed to $P^\sigma = m_p \delta^{\sigma 0}$. The squared amplitude of Eq. 33 reads;

$$|\mathcal{M}|^2 = \frac{2e^2 |M_P|^2}{q^2} m_p^2 \left[\varepsilon_{\mu\nu\rho\sigma} \varepsilon^{\mu\nu}_{\rho'\sigma'} q^\rho q^{\rho'} - \frac{4}{q^2} \varepsilon_{\mu\nu\rho\sigma} \varepsilon^\mu_{\nu'\rho'\sigma'} p_+^\nu p_+^{\nu'} q^\rho q^{\rho'} \right] \quad (34)$$

The sign change is due to $g^{\sigma\sigma'} = -\delta^{\sigma\sigma'}$. Using the antisymmetric tensor properties $\varepsilon_{\mu\nu\rho\sigma} \varepsilon^{\mu\nu}_{\rho'\sigma'} = 2\delta_{\rho\rho'}$ and $\varepsilon_{\mu\nu\rho\sigma} \varepsilon^\mu_{\nu'\rho'\sigma'} = \delta_{\nu\nu'} \delta_{\rho\rho'} - \delta_{\nu\rho'} \delta_{\rho\nu'} = (\hat{e}_\nu \times \hat{e}_\rho) \cdot (\hat{e}_{\nu'} \times \hat{e}_{\rho'})$, Eq. 34 is reduced to

$$|\mathcal{M}|^2 = \frac{2e^2 |M_P|^2}{q^2} m_p^2 \left[2|\mathbf{q}|^2 - \frac{4}{q^2} |\mathbf{q}|^2 |\mathbf{p}_+|^2 \sin^2(\theta_{p_+q}) \right] \quad (35)$$

A.2.2 Decay rate

The decay rate of a three-body decay is given in Equation 46.19 of [55] as

$$d\Gamma = \frac{1}{(2\pi)^5} \frac{1}{16m_p^2} |\mathcal{M}|^2 |\mathbf{p}_1^*| |\mathbf{p}_3| d\Omega_1^* d\Omega_3 dm_{12}, \quad (36)$$

where $(|\mathbf{p}_1^*|, \Omega_1^*)$ is the momentum of particle 1 in the rest frame of 1 and 2, and Ω_3 is the angle of particle 3 in the rest frame of the decaying particle m_p [55]. Relating Eq. 36 to the variables in Eq. 35, where $(|\mathbf{p}_1^*|, \Omega_1^*) = (|\mathbf{p}_+|, \Omega_{p_+q})$, $m_{12} = q$ and $(|\mathbf{p}_3|, \Omega_3) = (|\mathbf{p}_k|, \Omega_k)$, reads;

$$d\Gamma = \frac{1}{(2\pi)^5} \frac{1}{16m_p^2} |\mathcal{M}|^2 |\mathbf{p}_+| |\mathbf{p}_k| d\Omega_+ d\Omega_k dq, \quad (37)$$

In the rest from of the decaying particle m_p , the 3-momenta $|\mathbf{p}_k| = |\mathbf{q}|$ and the solid angle $\Omega_k = \Omega_q$. Substituting the square matrix element from Eq. 35 into Eq. 37 yields;

$$d\Gamma = \frac{1}{(2\pi)^5} \frac{1}{16m_p^2} \frac{2e^2 |M_P|^2}{q^2} m_p^2 \left[2|\mathbf{q}|^2 - \frac{4}{q^2} |\mathbf{q}|^2 |\mathbf{p}_+|^2 \sin^2(\theta_{p_+q}) \right] \times [\\ |\mathbf{p}_+| |\mathbf{q}| d\Omega_{p_+q} d\Omega_q dq] \quad (38)$$

The variables $|\mathbf{q}|$ and $|\mathbf{p}_+|$ can be redefined, by means of Eq. 46.20b and Eq. 46.20a of [55], as

$$|\mathbf{q}| = \frac{m_p^2 - q^2}{2m_p} \quad (39)$$

$$|\mathbf{p}_+| = \frac{\sqrt{q^2 - 4m_l^2}}{2} = \frac{q\sqrt{1 - \frac{4m_l^2}{q^2}}}{2} = \frac{q\mathcal{K}}{2}, \quad (40)$$

where $\mathcal{K} = \sqrt{1 - \frac{4m_l^2}{q^2}}$. Replacing the variables calculated in Eq. 39 and Eq. 40 into Eq. 38 and collecting terms yields;

$$d\Gamma = \frac{1}{(2\pi)^5} \frac{1}{16m_p^2} |M_P|^2 \left[\frac{2e^2 m_p^2}{8} \left(\frac{m_p^2 - q^2}{2m_p} \right)^3 \right] \times [\quad (2 - \mathcal{K}^2 \sin^2(\theta_{p_+q})) \frac{\mathcal{K}}{4q^2} dq^2 d\Omega_{p_+q} d\Omega_q] , \quad (41)$$

where the identity $q dq = \frac{dq^2}{2}$. Performing the integration of $\Omega_{p_+q} d\Omega_q$ and replacing $e^2 = 4\pi\alpha$ transforms Eq. 41 into;

$$d\Gamma = \frac{1}{(2\pi)^3} \frac{1}{32} \frac{4\pi\alpha}{3} |M_P|^2 \left[\frac{m_p^6 \left(1 - \frac{q^2}{m_p^2}\right)^3}{m_p^3} \right] (3 - \mathcal{K}^2) \frac{\mathcal{K}}{q^2} dq^2 , \quad (42)$$

which can be simplified further to;

$$d\Gamma = \left(\frac{1}{64\pi} |M_P|^2 m_p^3 \right) \frac{2\alpha}{3\pi} \frac{1}{q^2} \left(1 - \frac{q^2}{m_p^2}\right)^3 \left(1 + \frac{2m_l^2}{q^2}\right) \left(1 - \frac{4m_l^2}{q^2}\right)^{\frac{1}{2}} dq^2 . \quad (43)$$

It can be seen that the first set of variables in parenthesis in Eq. 43 is Eq. 27, therefore;

$$\frac{d\Gamma}{\Gamma_{\gamma\gamma} dq^2} = \frac{2\alpha}{3\pi} \frac{1}{q^2} \left(1 - \frac{q^2}{m_p^2}\right)^3 \left(1 + \frac{2m_l^2}{q^2}\right) \left(1 - \frac{4m_l^2}{q^2}\right)^{\frac{1}{2}} \quad (44)$$

which is the Kroll-Wada equation founded in [27].

B Tabular Rates

Table 6 gives expected count rate for several bins of $M(e^+e^-)$ for a torus field setting of 75%. Table 7 gives expected count rate for several bins of $M(e^+e^-)$ for a torus field setting of 100%.

$M(e^+e^-)$ Bin Center	Upper ($\epsilon_\gamma = 10\%$)	Uncertainty	Lower ($\epsilon_\gamma = 2\%$)	Uncertainty
0.01	8924	94	946	31
0.03	1720	41	180	13
0.05	1041	32	113	11
0.07	758	28	84	9
0.09	578	24	62	8
0.11	479	22	54	7
0.13	411	20	45	7
0.15	369	19	37	6
0.17	329	18	36	6
0.19	317	18	36	6
0.21	280	17	30	5
0.23	268	16	28	5
0.25	250	16	26	5
0.27	269	16	28	5
0.29	266	16	24	5
0.31	250	16	25	5
0.33	240	15	24	5
0.35	258	16	25	5
0.37	309	18	31	6
0.39	280	17	28	5
0.41	352	19	35	6
0.43	285	17	31	6
0.45	299	17	31	6
0.47	315	18	34	6
0.49	328	18	35	6
0.51	326	18	38	6
0.53	331	18	30	5
0.55	282	17	28	5
0.57	401	20	38	6
0.59	416	20	45	7
0.61	438	21	48	7
0.63	445	21	44	7
0.65	448	21	44	7
0.67	577	24	63	8
0.69	689	26	69	8
0.71	728	27	79	9
0.73	716	27	71	8
0.75	706	27	73	9
0.77	565	24	54	7
0.79	277	17	29	5
Total	26521	163	2784	53

Table 6: Counts rates for bins of $M(e^+e^-)$ at 75% torus field. ϵ_γ is the photon detection efficiency.

$M(e^+e^-)$ Bin Center	Upper ($\epsilon_\gamma = 10\%$)	Uncertainty	Lower ($\epsilon_\gamma = 2\%$)	Uncertainty
0.01	7937	89	859	29
0.03	1516	39	163	13
0.05	934	31	102	10
0.07	684	26	77	9
0.09	501	22	56	7
0.11	392	20	45	7
0.13	366	19	40	6
0.15	335	18	34	6
0.17	276	17	31	6
0.19	266	16	30	5
0.21	246	16	28	5
0.23	238	15	25	5
0.25	218	15	22	5
0.27	245	16	26	5
0.29	225	15	21	5
0.31	218	15	22	5
0.33	217	15	22	5
0.35	226	15	23	5
0.37	275	17	29	5
0.39	256	16	27	5
0.41	292	17	31	6
0.43	274	17	29	5
0.45	262	16	26	5
0.47	244	16	27	5
0.49	296	17	32	6
0.51	303	17	36	6
0.53	295	17	28	5
0.55	255	16	26	5
0.57	338	18	33	6
0.59	381	20	43	7
0.61	382	20	43	7
0.63	399	20	41	6
0.65	419	20	41	6
0.67	527	23	57	8
0.69	597	24	62	8
0.71	695	26	76	9
0.73	664	26	68	8
0.75	657	26	68	8
0.77	545	23	54	7
0.79	271	16	28	5
Total	23667	154	2528	50

Table 7: Counts rates for bins of $M(e^+e^-)$ at 100% torus field. ϵ_γ is the photon detection efficiency.